Los Alamos NATIONAL LABORATORY EST.1943

LA-UR-15-22836 (Accepted Manuscript)

Mixing transition in a shocked variable-density flow

Orlicz, Gregory Christopher
Balasubramanian, Sridhar
Vorobieff, Peter
Prestridge, Katherine Philomena

Provided by the author(s) and the Los Alamos National Laboratory (2019-01-09).

To be published in: Physics of Fluids

DOI to publisher's version: 10.1063/1.4935183

Permalink to record: http://permalink.lanl.gov/object/view?what=info:lanl-repo/lareport/LA-UR-15-22836

Disclaimer:
Approved for public release. Los Alamos National Laboratory, an affirmative action/equal opportunity employer, is operated by the Los Alamos National Security, LLC for the National Nuclear Security Administration of the U.S. Department of Energy under contract DE-AC52-06NA25396. Los Alamos National Laboratory strongly supports academic freedom and a researcher's right to publish; as an institution, however, the Laboratory does not endorse the viewpoint of a publication or guarantee its technical correctness.

RESEARCH LIBRARY

Mixing transition in a shocked variable-density flow.

G.C. Orlicz,[1] S. Balasubramanian,[2] P. Vorobieff,[3] and K.P. Prestridge[1, a)]

[1)] *Extreme Fluids Team, P-23, Physics Division, Los Alamos National Laboratory, Los Alamos, NM, 87545, USA*

[2)] *Department of Mechanical Engineering, Indian Institute of Technology, Bombay, Mumbai, MH, 400076, India*

[3)] *Department of Mechanical Engineering, University of New Mexico, Albuquerque, NM 87131, USA*

(Dated: 23 October 2015)

We measure two-dimensional velocity and density fluctuations in a shock-driven heavy gas curtain for three different incident Mach numbers (M = 1.21, 1.36, and 1.50) and a fixed initial perturbation. We study the time evolution of the velocity and density fields and observe two different mixing transitions in this unsteady flow. The first transition is caused by small-scale mixing in vortex cores, while the second transition is related to increased homogenization across the mixing layer and a drive towards isotropy. By measuring the anisotropy of the velocity fluctuations and the evolution of the turbulent kinetic energy, we are able to assess the anisotropy of the flow. For the first time in Richtmyer-Meshkov (RM) flows, we measure and compare turbulent length scales derived from both the density and velocity field measurements, and we find ratios of Liepmann-Taylor to inner-viscous scales (λ_L/λ_ν) that are inconsistent with those found using Reynolds number scaling based on circulation, Re_Γ, or based on turbulent kinetic energy, Re_K. At late times, Re_K better reflects the decay of the mixing field than Reynolds numbers that are based upon mixing width or circulation. We also estimate the time evolution of dissipation and Kolmogorov scales for the first time in RM flows. When we estimate the Taylor microscale (λ_T) for our experiments using both density and velocity, the density microscale agrees well with with the relationship $\lambda_T = \sqrt{10}\delta \mathrm{Re}^{-1/2}$ where $Re = Re_K$ and δ is the mixing layer width, but the velocity-based Taylor microscale follows a new scaling of $\lambda_T = 10\delta \mathrm{Re}^{-1/2}$.

[a)] kpp@lanl.gov; http://www.lanl.gov/projects/shocktube/

I. INTRODUCTION

The Richtmyer-Meshkov instability (RMI)[1,2] is a focus of experimental, theoretical and numerical work for the important role it plays in driving fluid mixing in both naturally occurring phenomena, such as supernovae[3] and in the magnetosphere[4], and in engineering applications, such as inertial confinement fusion (ICF)[5,6] and supersonic combusting ramjet engines[7]. The RMI occurs when a perturbed fluid interface between two fluids of different densities is impulsively accelerated, commonly by a shock wave. The misalignment of pressure and density gradients generates baroclinic vorticity that drives the growth of the instability. The variable-density nature of RMI flows is a complicating factor in efforts to model the behavior of these flows as they transition toward turbulence. In variable density mixing, the scalar mixing state actively modulates the flow dynamics, called "Level-2 mixing"[8]. Therefore, the characteristics of the subsequent mixing are different when compared to those generated by classical turbulence.

Another complicating effect is the unsteadiness of shock-driven mixing. At early times, fluid motion occurs at scales comparable to those of the initial perturbations. As time progresses, given sufficient energy deposition by the impulsive acceleration, the flow may transition to smaller scale fluid motions as secondary instabilities arise, and larger scale vortices break down into smaller ones, enhancing fluid mixing.

A framework for assessing the transitional mixing state in RMI induced flows has been established in recent work[8–12]. For a flow to transition to turbulence, two possible criteria[9] are that the flow must reach a Reynolds number, $\mathrm{Re} > 10^4$, or a Taylor Reynolds number, $\mathrm{Re}_T > 100$. Most of the problems considered for establishing the criteria were statistically stationary flows, such as turbulent jets and boundary layers. For temporally evolving transitional RMI flows that lack additional energy input after the initial impulse, it remains an open question how Reynolds number should be defined and how to apply or define transition criteria. With recent advances in diagnostic capabilities, some experimentalists have focused on quantifying the turbulence quantities and length scales that have been identified as important for characterizing the nature of the RMI induced mixing[13–18].

In the present work, simultaneous particle image velocimetry (PIV) and quantitative planar laser induced fluorescence (PLIF) are used to study the evolution of a shocked heavy gas curtain. We focus on the mixing transition that occurs as a result of the growing RMI for 3

incident shock Mach number cases ($M = 1.21$, 1.36, and 1.50). With measurements at over 40 different times for each Mach number, we investigate the flow with unprecedented temporal resolution for experimental studies of RMI. At some times we have enough individual realizations for ensemble averaged statistics, permitting a comparison to statistics derived from instantaneous spatial averages. Metrics are presented to assess the state of the mixing layer throughout time, to determine whether the flow meets certain transition criteria for turbulence, and to evaluate the appropriateness of those criteria for this particular flow. For the first time in experimental RMI flows, we show a detailed time evolution of estimates of turbulent kinetic energy, and several turbulent length scales, including both density and velocity based Taylor microscales, with attention given to signatures of different mixing transitions that these quantities indicate. This article is complementary to that found in Orlicz *et al.*[19] that focused on the scalar mixing state for the same set of experiments. In the present work, more attention is given to information extracted from the velocity fields to show the highly resolved time evolution of turbulence related quantities, how they can be scaled between different Mach number experiments, and how they differ depending on the method used to estimate them.

While in this work, we investigate the effect of changing Mach number, our group has reported some of these turbulence related quantities previously when initial conditions are changed[15] or in the presence of reshock[13,16,20]. We would also like to point attention to numerical work that has focused on the evolution of turbulence related quantities in RMI flows when Mach number is changed[12,21], initial conditions are changed[22–26], and in the presence of reshock[21,22,26,27]. For more general theoretical work on the physics of variable density turbulent mixing we recommend Livescu and Ristorcelli[28].

II. EXPERIMENTAL PROCEDURES AND UNCERTAINTY ESTIMATES

The experiments were performed at the Los Alamos horizontal gas shock tube. A schematic of the shock tube and a detailed description of its operation can be found in previous work[19,29]. The initial conditions consist of a thin, varicose perturbed, heavy gas curtain surrounded by air. The heavy gas is a mixture of sulfur hexafluoride (SF_6), air, acetone, and glycol droplets. The glycol droplets have been previously measured in earlier experiments at the facility to have a mean diameter of about 0.5 μm. The heavy gas mixture

is allowed to flow by gravity through a special nozzle with an exit aligned with the top wall of the shock tube. The resulting row of closely spaced jets that flow through the test section make up the gas curtain initial conditions with a perturbation wavelength of $\lambda = 3.6$ mm. At the primary x-y measurement plane located 2 cm below the top wall of the shock tube, the peak SF_6 volume fraction along the center line of the curtain is estimated to be $\approx 45\%$, with 12% acetone vapor and 43% air by volume (see Orlicz *et al.*[19]). The Atwood number for this mixture composition is $A = 0.49$, where $A = (\rho_2 - \rho_1)/(\rho_2 + \rho_1)$, and ρ_1 and ρ_2 are the densities of the surrounding air and the heavy gas mixture, respectively. A numerical representation of the 2-D initial condition profile can be found in Orlicz *et al.*[19], as well as many other experimental configuration details and image processing methods.

Density and velocity measurements were obtained using two dual headed pulsed lasers with output wavelengths of 266 nm for PLIF, and 532 nm for PIV. The lasers are co-aligned and formed into sheets, with the 266 nm frequency causing the acetone tracer to fluoresce, while the 532 nm is scattered off of the fog droplets. PIV image pairs were processed using Insight 3G software (ver 9.1.0.0) with a recursive Nyquist processor with final window size of 24×24 pixels. This provided a velocity vector spacing of 193 μm/vector. The resolution of the PLIF based density measurements is 50.5 μm/pixel.

Uncertainty in our PLIF measurements has been addressed previously[13,15] and is relevant to the current results. The largest single source of uncertainty is associated with our conservation of mass assumption that the amount of heavy gas in the measurement volume of the initial conditions is the same as that in an equal sized measurement volume of the post-shock conditions (see Orlicz *et al.*[19] for details of this method). We found the amount of heavy gas in the initial conditions to vary by about $\pm$ 3%, and this statistical uncertainty propagates to our post-shock measurements. Net flow of heavy gas in or out of the measurement volume over time is an additional source of uncertainty that cannot be quantified by the planar measurements in the current work, but is expected to be smaller than the statistical variation of the initial conditions. Other sources of uncertainty result from the initial calibration using the test cell[19], pulse to pulse laser sheet profile variations, image resolution, and pixel response. We estimate these effects to contribute to $\pm$ 4% measurement uncertainty. Since the statistical and measurement uncertainties are uncorrelated, we add them in quadrature and estimate the total uncertainty within a given density map to be $\pm$ 5%. The measurement uncertainty is drastically reduced when the measurements pre-

sented represent averages of the field (around 10,000 pixels are used for many of the spatial averages), and the statistical uncertainty is reduced when ensemble averages are used, both by a factor of $\frac{1}{\sqrt{n}}$ where n is the number of points used for averaging.

The common sources of PIV uncertainty are limitations in spatial and temporal resolution, tracer tracking fidelity, the correlation algorithms used, and any smoothing/interpolation in postprocessing. Our group has published several papers that discuss the uncertainty associated with PIV measurements[13,15,29]. For the present work, similar PIV parameters and processing techniques are used as discussed in those papers. For spatial resolution, we assume an uncertainty in the location of a particle to be half the pixel size. The pixel resolution of PIV images was 16.1 μm/pixel. When this uncertainty is added in quadrature, the displacement uncertainty for a single particle is 11.4 μm. With about 10 peaks in a typical correlation window, the displacement uncertainty associated with a given vector is (11.4 μm)/$\sqrt{10}$ = 3.6 μm, and therefore a 3.6 m/s velocity uncertainty for Mach 1.36 and 1.50 experiments with Δt = 1 μs. Uncertainties due to the temporal resolution are estimated to be small compared to the spatial resolution. The effect of averaging over many vectors greatly reduces the uncertainty of the final results. For the quantities that we average over the middle 20% of the mixing layer, somewhere around 1200 vectors are used. Dividing by $\sqrt{n}$ for averaged quantities gives an uncertainty of about 3.6 m/s / $\sqrt{1200}$ = 0.1 m/s, or about 2% of the root mean squared velocity fluctuation level at late times.

Next, we address the uncertainties associated with processing and postprocessing. It was found that the number of interpolated/filled vectors was around 5%. However, it is important to note that a majority of these interpolated vectors were near the edges of the mixing layer where the seeding density is typically low. In our analysis, several of the quantities given were only from those locations making up the middle 20% of the mixing layer. At those locations, the rejection/interpolation was much lower (approximately 1%) and contributes a small effect to the overall results. A 5×5 Gaussian filter with $s = 0.8$ was used for smoothing, but it was found to also have a small 2% effect on the velocity statistics when compared to fields without smoothing.

The question of particle tracking fidelity applies both to turbulent[30–32] and to shock-accelerated[33] flow. The response time of the particles to reach the piston velocity in Mach 1.50 experiments is estimated to be about 10 μs using various drag models[34,35]. Our earliest PIV measurements are reported for times much later at 225 μs after shock interaction, so

the shock-accelerated lag does not effect our results. For turbulent lag (i.e. the ability of particles to accurately follow the velocity fluctuations), we follow Elghobashi[32] and find that the response time of particles is small compared to our estimates of both the eddy turnover time and the Kolmorgorov time scale (about 1% and 4%, respectively). Consequently, we expect the particles to follow the flow well throughout the times our measurements were made. Also, with the small volume fraction of droplets ($\sim 10^{-9}$), the presence of the droplets should not have a significant effect on the turbulence[32].

A discussion about how the uncertainties in our PLIF and PIV data propagate to uncertainties in several turbulence quantities can be found in Balakumar *et al.*[13]. For more discussion of PIV uncertainty, we point to additional resources[18,36–38].

III. RESULTS

Using two PLIF pulses and one PIV image pair per run of the experiment, a time evolution can be constructed from multiple runs of the experiment. Multiple experiments were performed at each time, providing multiple realizations of both density and velocity fields that we use for statistical averaging. A small selection of PLIF based SF_6 concentration maps showing the evolution of the gas curtain with time are presented in Figure 1. A complete time evolution is available in Orlicz *et al.*[19]. Images along a row show the mixing layer at the same streamwise distance from the initial conditions for each Mach number and correspond to scaled time. At early times, up to $x \approx 6$ cm, the evolution of the curtain appears similar for each Mach number. Throughout intermediate times, from 6 cm to 13 cm, the fluid mixing layers begin to grow differently and begin to exhibit smaller scale mixing primarily near the vortex cores. At late times, $x > 13$ cm, the mixing layers become increasingly disordered with more apparent small scale mixing, and the differences observed at intermediate times become more enhanced. By the latest times visualized, the mixing layers exhibit a wide range of scales hinting that the flow is transitioning toward turbulence. A full analysis of the scalar mixing field is presented in[19].

Figure 2 shows simultaneous velocity and density field data for Mach 1.36 experiments. From left to right, the columns are PLIF SF_6 volume fraction maps, vorticity fields ($\vec{\omega_z} = \partial\vec{v}/\partial x - \partial\vec{u}/\partial y$), and estimations of turbulent kinetic energy, K, defined later in Section III B. The latter two quantities help us understand the energy transfer and rate of energy decay,

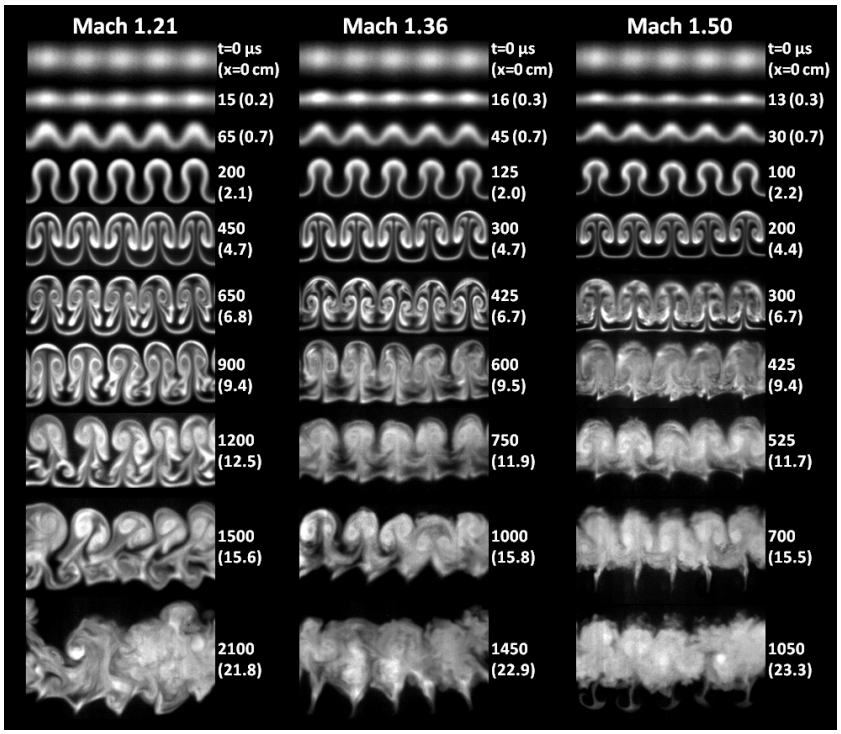

FIG. 1. A selection of SF_6 volume fraction maps from each Mach number experiment. Images in each row were acquired at roughly the same location as indicated in the figure, with time t and distance traveled (x). Contrast adjusted for optimizing visualization for each image.

and how that impacts the mixing observed in the density fields. As time progresses, the array of alternating blobs of positive and negative vorticity begin to lose their symmetry, leading to a transition of the vorticity field to a more disordered state, and a break up of the main vortices into smaller ones, indicating an energy cascade.

A. Velocity fluctuations

In this section we present velocity fluctuations both from spatially averaged and ensemble averaged mean values. The results are compared between Mach number as these quantities evolve in time. Figure 3 shows streamwise and spanwise RMS velocity fluctuations from the spatial average as a function of streamwise position at early and late times for each Mach number. The velocity fluctuations, u' and v', were calculated from an instantaneous realization by first computing $\bar{u}$ and $\bar{v}$, the whole field mean of the streamwise and spanwise velocity fields, respectively

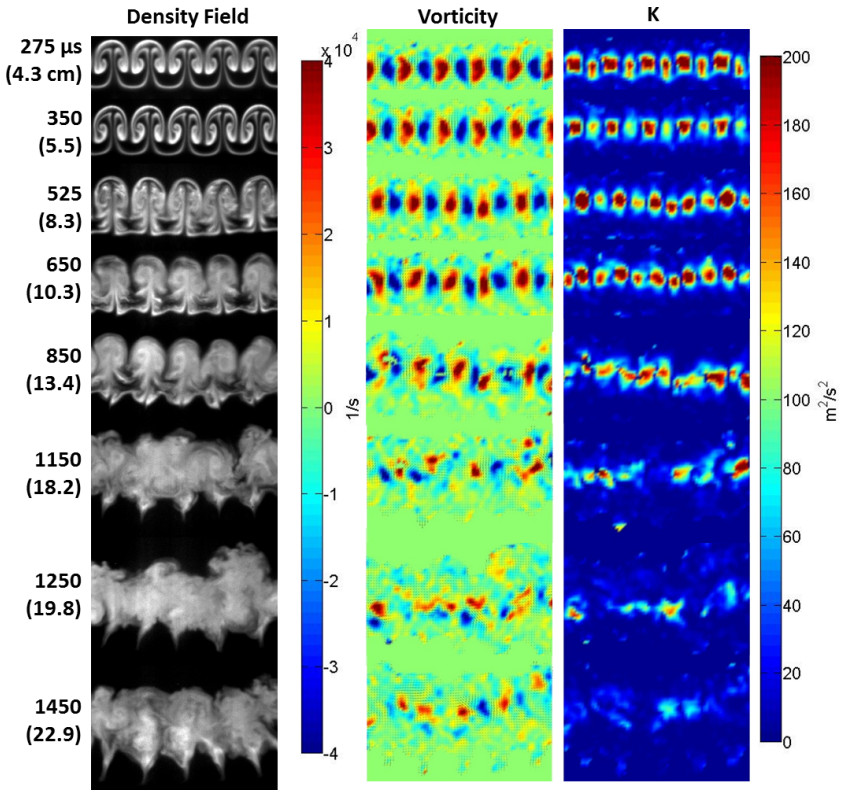

FIG. 2. Demonstration of simultaneous PIV/PLIF data for Mach 1.36 experiments.

$$u'(x,y) = u(x,y) - \bar{u} \quad , \quad v'(x,y) = v(x,y) - \bar{v}. \tag{1}$$

Then σ_u and σ_v were calculated for each streamwise position within the mixing layer by taking the root-mean-square (RMS) of the fluctuations along the spanwise direction so that

$$\sigma_u(x) = \sqrt{\overline{u'^2(x,y)}^{\,y}} \quad , \quad \sigma_v(x) = \sqrt{\overline{v'^2(x,y)}^{\,y}}, \tag{2}$$

where the subscript y on the overbar indicates spanwise averaging. For each Mach number case, at earlier times the velocity fluctuations are about 3 times higher in the streamwise direction with a peak at the center of the mixing layer, while there is a local minimum in the spanwise fluctuations at the same location. These features can be explained by considering the primary vortices that dominate the mixing layer at these early times. It is at the streamwise center of the main vortices where the streamwise velocity has the highest and lowest values, and therefore the highest fluctuations from the spatially averaged mean flow. The local minimum in the spanwise fluctuations occurs because along the streamwise center of a vortex the absolute value of the spanwise velocity is relatively low. Note that the mean

spanwise velocity is zero owing to the spanwise symmetry of the flow.

At later times, the peaks in the velocity fluctuation profiles disappear, indicating that the velocity field is becoming more disordered. This observation corresponds to the qualitative breakdown observed in the vorticity fields. At late times, the streamwise and spanwise fluctuations have comparable values, showing increasing isotropy in the measured components.

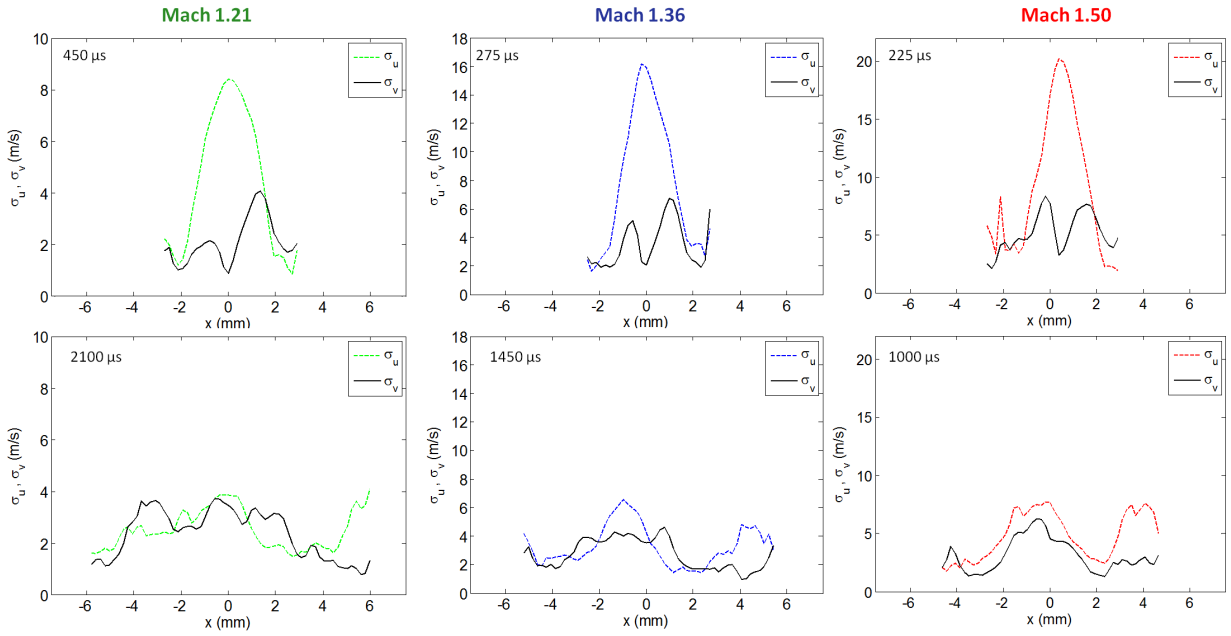

FIG. 3. Variation of velocity fluctuations with streamwise location for each Mach number: at early time (top row) and late time (bottom row).

Probability density functions (PDFs) for the fluctuations from instantaneous spatial averages of both components of velocity, u' and v', are presented in Figure 4. Because turbulence is characterized by large intermittent fluctuations in velocity, the PDFs in a developing turbulent flow tend to develop non-Gaussian profiles with long tails[39]. Non-Gaussian profiles with long tails are observed at earlier times for the streamwise component, u', for all three Mach numbers.

The PDFs of the spanwise component, v', have relatively short tails even at early times. The PDFs of v' also tend to be symmetric about the mean, due to the spanwise symmetry of the flow. However, at earlier times the PDFs of u' tend to be asymmetric with a higher probability for extreme negative (upstream) fluctuations than for extreme positive fluctuations. This indicates that the direction of the shock is still imprinted on the flow at early times. As time progresses, both distributions become increasingly narrow about the 0

value, and the PDFs for u' become more symmetric with much shorter tails, an indication of decaying turbulence. That the profiles of both the u' and v' PDFs are similar at late times also indicates the flow is tending toward isotropy in the two measured components. As a function of Mach number, the PDFs of both u' and v' are wider with increasing M for a given scaled time, x, reflecting the higher fluctuations that result from higher Mach number shock waves.

The use of instantaneous realizations to estimate turbulence levels is useful for validation of numerical simulations where averages must also be obtained from a single realization. In many shock-driven and unsteady experiments, it is also not practical to acquire enough data for statistical convergence, and spatial averaging can be used to calculate fluctuating quantities. An advantage in these single-mode initial conditions is that the spanwise repetitiveness of the flow lends itself to averaging over each wavelength, providing more data for constructing a local ensemble average. Using this technique, mean values ($\langle u(x,y)\rangle$ and $\langle v(x,y)\rangle$) were obtained by phase averaging over the individual wavelengths from multiple realizations taken at the same post-shock time. PDFs showing u' and v' from these ensemble average mean quantities are shown in Figure 5. Note that the rows in Figure 5 are not at the same scaled time as they are in Figure 4. A slightly different story of the mixing emerges from Figure 5. At the earliest times shown, there is anisotropy in the streamwise and spanwise components (similar to Figure 4), and at the latest times the profiles of the two components are nearly identical indicating that the flow is developing isotropy (similar to Figure 4). But here the profiles showing the strongest fluctuations occur at the middle time shown. In general, the PDFs start out narrower, widen, and then become narrower again. This occurs for both u' and v' in Mach 1.36 experiments. For example, the PDF of v' is very similar at 375 μs and 1500 μs, and is wider at intermediate time 850 μs. The trend observed in the ensemble averaged PDFs in Figure 5 better reflects the observed flow behavior. The passage of the shock wave through the curtain initially results in a primarily inviscid, vortex-dominated flow. Then as a result of vortex core breakdown, the mixing layer becomes turbulent. As time progresses, the turbulent energy decays resulting in reduced turbulence intensities (reduced intermittency levels of both u' and v'). Note that over early and intermediate times there is transfer of energy from the streamwise fluctuating component to the spanwise component, which results in the widening of the v' PDF observed at the intermediate time shown.

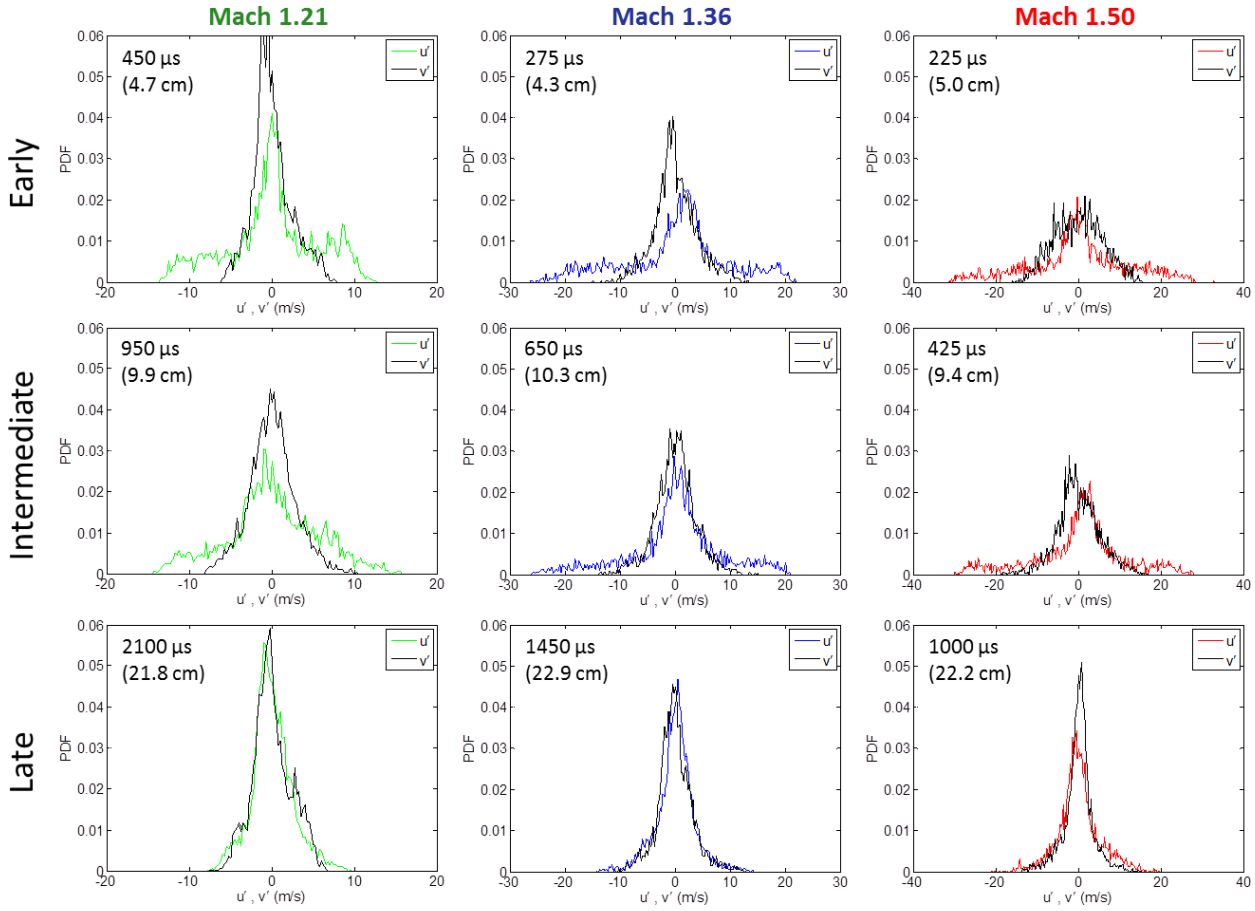

FIG. 4. PDFs for velocity fluctuations computed using instantaneous spatial averaging for each Mach number at early, intermediate, and late time.

B. Turbulent kinetic energy estimates

From the velocity fluctuations, we estimate the turbulent kinetic energy (K) field due to velocity components in the plane of visualization as

$$K(x,y) = \frac{1}{2}(u'^2(x,y) + v'^2(x,y)). \tag{3}$$

The full turbulent kinetic energy field would have to include fluctuations of all three velocity components. However, our reconstructions can likely be aided by the inherently three-dimensional nature of transition to turbulence, as in the limit case of fully developed isotropic turbulence the out-of-plane velocity fluctuations would have statistics similar to those of the streamwise and spanwise component. In our transitional flow, determination of the exact relationship between turbulent kinetic energy and our two-component estimate remain a task for the future. However, we may assume that the estimates from Eq. 3 represent a

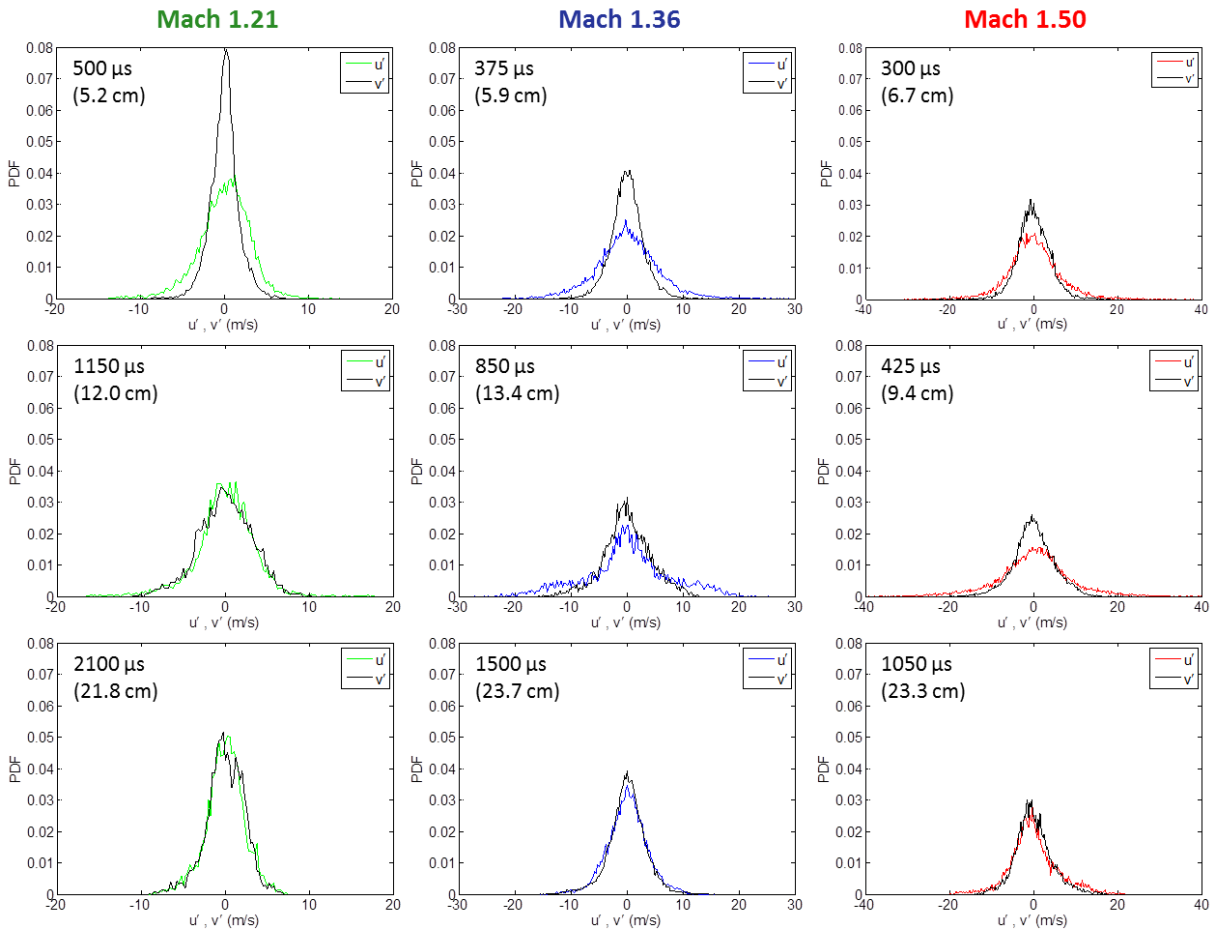

FIG. 5. PDFs for velocity fluctuations computed using the ensemble phase averaging for each Mach number.

lower bound on our measured values. As an upper bound, since most of the initial energy is deposited in the two in plane components, we can assume that the out of plane fluctuations, w', are no higher than those in v' so that $K(x,y) = \frac{1}{2}(u'^2(x,y) + 2v'^2(x,y))$. $K(x,y)$ fields obtained using both instantaneous spatial averaging and ensemble phase averaging are shown in Figure 6(a) using Eq. 3. The evolution of the mean value of K estimates, $\overline{K(x,y)}$, is shown for each Mach number using both methods as a function of scaled time ($x = \Delta u\, t$). The overbar indicates whole-field spatial averaging of the $K(x,y)$ field.

Turbulence levels, as indicated by $\overline{K(x,y)}$ are initially proportional to Mach number, as shown in Figure 6(a). If $\overline{K}$ is nondimensionalized using the velocity jump imparted on the interface squared, Δu^2, the data from the different Mach number cases collapse fairly well for both instantaneous and ensemble averaging techniques, as shown in Figure 6(b).

The collapse of K is achieved through use of a single parameter, Δu, applied to both axes. Δu reflects the primary difference in the driving input energy for the current flow (where only Mach number is varied). This scaling is worth exploring for universality in subsequent RMI Mach number studies. If other parameters that govern instability growth are varied between experiments (e.g., initial condition perturbation amplitude, wavenumber, or Atwood number), different factors such as the initial growth rate, $\dot{\delta}_0$, may need to be incorporated. In a study where the initial conditions were varied, Balasubramanian *et al.*[15] report a collapse of the K estimates amongst different single-mode configurations when scaled with $\dot{\delta}_0$. However, a collapse was not achieved between the single mode and multimode configurations, so the use of that scaling alone appears to be limited.

Differences between the two methods for estimating K are shown in Figure 6(b). Computed using an instantaneous spatially averaged basis, $\overline{K}$ is highest at earlier times and decreases as time progresses. The high values arise from the vortex-dominated structure of the mixing layer at early times that causes strong velocity variations from the spatially-averaged mean. $\overline{K}$ computed from an ensemble average should provide a better estimate of the true K present in the flow. In Figure 6(b), $\overline{K}$ from an ensemble average begins low, increases until it reaches a peak around $x = 13$ cm, and then decreases. This is consistent with what is known about the flow. After it is accelerated impulsively, it takes some time for energy to transfer out of the largest scales and into smaller-scale mixing motions. As this mixing transition occurs, $\overline{K}$ should increase. Without additional energy sources for the flow, we expect K to decrease as kinetic energy is lost through dissipation, and so we see an eventual decrease in $\overline{K}$.

When compared to ensemble average estimates, using an instantaneous average overpredicts K at earlier times. By $x = 13$ cm it appears to be a better estimate for each Mach number case. The $x \approx 13$ cm point at which the two methods begin to agree is also the location at which the ensemble-averaged estimates peak and seems to be an indication of a mixing transition in the flow. The agreement of the two methods throughout late time is also encouraging. This gives some validation to those who can only estimate K using spatial averages from an instantaneous field, provided there is other evidence that a mixing transition has occurred.

In Figure 7, we explore the convergence of $\overline{K}$ calculated from the ensemble averaging method. At each time reported, all wavelengths (5 for each realization) used for ensemble

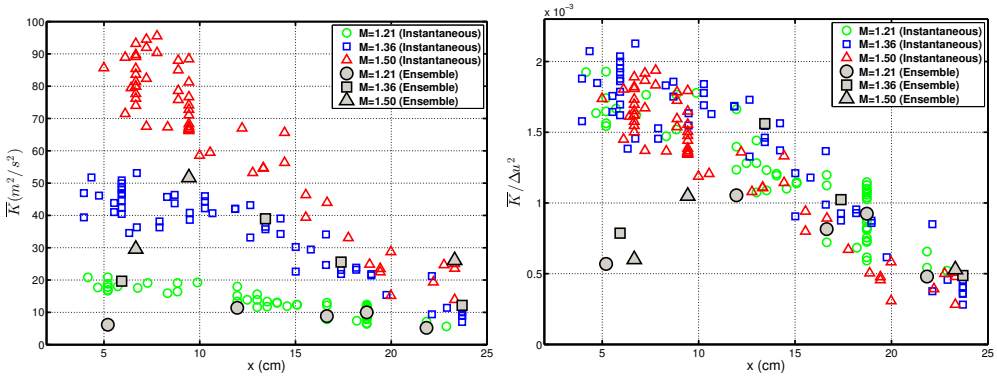

(a) (b)

FIG. 6. Comparison of (a) $\overline{K}$, and (b) $\overline{K}/\Delta u^2$ as a function of scaled time when calculated from spatially averaged instantaneous realizations (color) *vs* ensemble averaged fields (grey).

averaging were placed in a randomized order to avoid any biasing of the convergence from wavelengths within a given realization. $\overline{K}$ was then computed by sequentially adding one wavelength at a time to the averaging process. Figure 7 shows the convergence for 2 different times in each Mach number case. We find that the number of wavelengths required for convergence varies with Mach number and time, but reasonably good convergence requires 30 to 50 wavelengths (6 to 10 separate realizations in our case) for most of the times investigated, with some requiring more (e.g. M =1.21, t = 1800 µs).

C. Reynolds numbers

In unsteady RMI flows, the length scales and velocities are continuously evolving. Due to these unsteady effects, Re should be chosen judiciously to reflect the flow dynamics at the times of interest. We explore three different Reynolds number calculations to quantitatively determine their usefulness in characterizing and understanding Richtmyer-Meshkov instabilities. Re is defined using total mixing width growth rate, $\dot{\delta}$, the average circulation of the vortices, Γ, and the turbulent kinetic energy $\overline{K}$:

$$\mathrm{Re}_\delta = \frac{\delta\dot{\delta}}{\nu} \quad , \quad \mathrm{Re}_\Gamma = \frac{\Gamma}{\nu} \quad , \quad \mathrm{Re}_K = \frac{\sqrt{\overline{K}}\delta}{\nu}. \tag{4}$$

The kinematic viscosity, ν, was calculated using an average mixture composition across

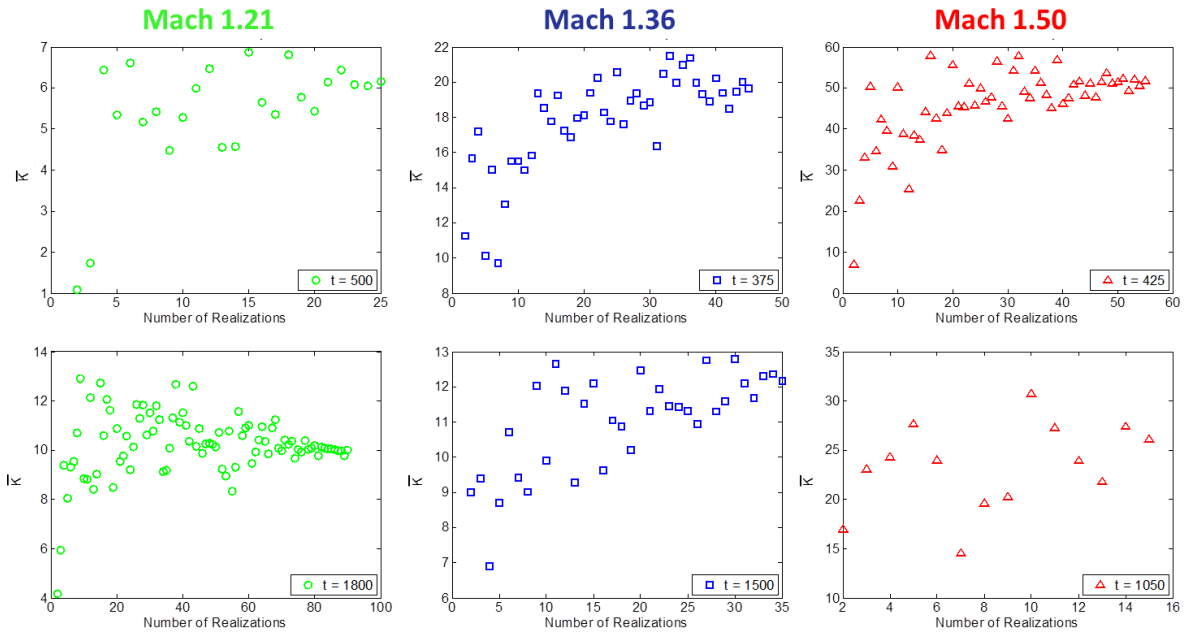

FIG. 7. Demonstration of various levels of convergence for the calculation of the ensemble based $\overline{K}$ with increasing number of wavelengths used for averaging. Times are in μs.

the mixing layer at post-shock conditions for each post-shock time following the method of Reid[40] for the viscosity of gas mixtures. Figure 8 shows the evolution of ν over scaled time, a calculation that has not previously been considered in RMI experiments but is important because ν increases by approximately 60% over the duration of these measurements. The total mixing layer width of the density fields, δ, was measured using the technique described in Orlicz *et al.*[19]. In Figure 9(a), Re_δ does not show obvious differences between Mach numbers and contains a lot of scatter because the measurement of the growth rate at each time is affected by small perturbations. Re_δ is useful during the linear stage of instability growth. The early time growth rates, $\dot{\delta}_0$, are 0.013, 0.029, and 0.042 mm/μs for $M = 1.21$, 1.36 and 1.50, respectively[19]. Early-time Re_δ, at $x = 0.7$ cm, are $\mathrm{Re}_\delta = 5200$, 13000, and 18500, for each Mach number.

Re_δ does not appear helpful for understanding the mixing physics of RMI flows after the earliest times. When flows with single-mode perturbations are dominated by rows of alternating vortices ($x < 13$ cm), circulation is a useful way to estimate mixing behavior. $\mathrm{Re}_\Gamma \approx 7000$, 12000, and 18000 for $M = 1.21$, 1.36, and 1.50, respectively for early and intermediate times (see Figure 9(b)). For $x > 13$ cm, when the primary vortices are less defined and the mixing layer appears to transition, $\mathrm{Re}_K \approx 2500$, 4000, and 6000 seems a more

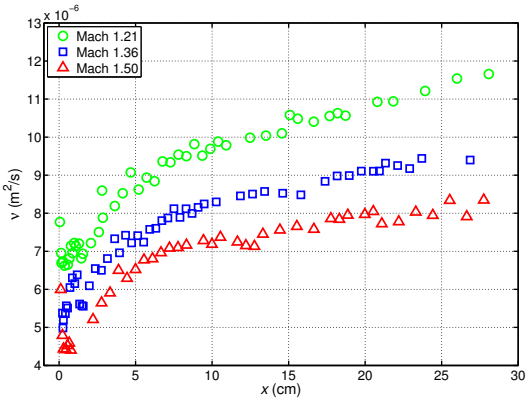

FIG. 8. Evolution of the average kinematic viscosity, ν, calculated using the mean mixture composition and the post-shock conditions at each measurement time.

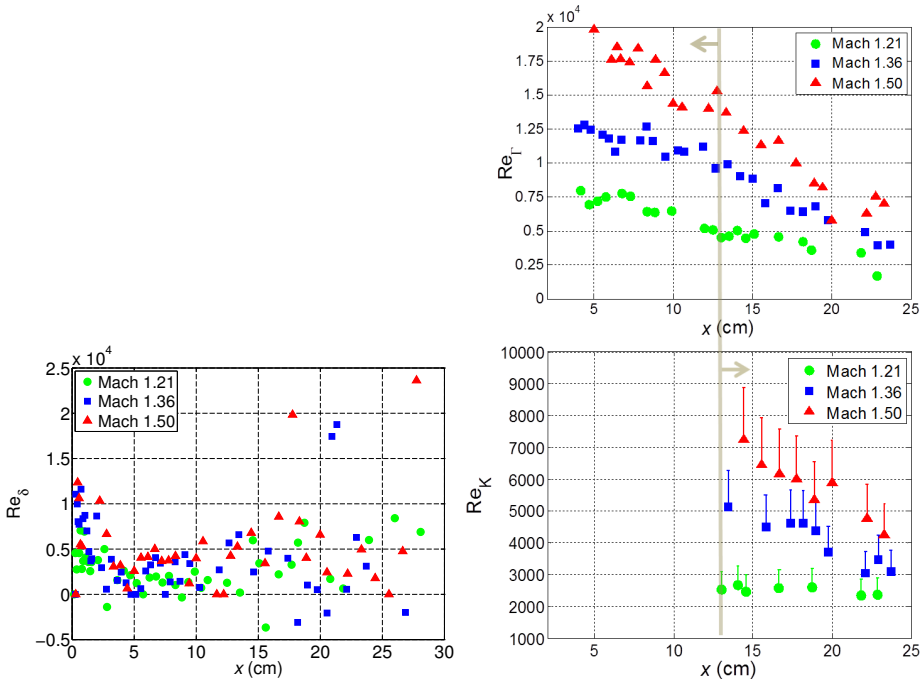

(a) (b)

FIG. 9. (a) Re_δ best describes the early-time, linear growth portion of the flow. (b)top: Re_Γ and (b)bottom: Re_K are useful for the times shown by the arrows. The symbols for Re_Γ and Re_K represent an average of all the realizations available at each time.

appropriate choice for understanding the flow. We propose that the use of one definition over another is time dependent. The error bar for Re_K represents the uncertainty associated with the fluctuation level of the out of plane component, w, since it was not measured. The upper bound was calculated assuming $w' = v'$ so that $K(x,y) = \frac{1}{2}(u'^2(x,y)+2v'^2(x,y))$. The commonly accepted minimum value for fully developed turbulence to occur[8,9] is $\mathrm{Re}_\Gamma = 10^4$. With these single-mode initial conditions, only Mach 1.36 and Mach 1.50 experiments meet this Re requirement, however all Mach numbers exhibit some signs of turbulence, particularly based on the Taylor Reynolds number, as will be discussed later.

D. Estimating turbulent length scales

1. Autocorrelation and Taylor Microscale

The Taylor microscale can be estimated for a turbulent flow from the curvature of the autocorrelations in the local region of the flow, $R(0)$, using either the density or velocity fluctuations. The autocorrelation is performed in the spanwise direction y such that,

$$R(r) = \frac{\langle \eta'(y)\eta'(y+r)\rangle}{(\eta')^2}, \tag{5}$$

where η' refers to either density, streamwise velocity fluctuations, or spanwise velocity fluctuations. The Taylor microscale is then,

$$\lambda_T = \Big[-\frac{1}{2}\frac{\mathrm{d}^2 R(0)}{\mathrm{d}r^2}\Big]^{-1/2}, \tag{6}$$

where $\lambda_{T,\rho}$, $\lambda_{T,u}$, and $\lambda_{T,v}$ refer to the density, streamwise velocity (transverse), and spanwise velocity (longitudinal) Taylor microscales, respectively. For the autocorrelations, density fluctuations and streamwise velocity fluctuations were found from the mean at each streamwise location ($\rho'(x,y) = \rho(x,y) - \overline{\rho(x)}^y$ and $u'(x,y) = u(x,y) - \overline{u(x)}^y$), whereas $v'(x,y) = v(x,y)$ owing to the spanwise symmetry of the flow ($\bar{v} = 0$). Figure 10, shows a $v'(x,y)$ field for a Mach 1.50 experiment at 1000 μs, and the corresponding autocorrelation at the streamwise center of the mixing layer. Also shown is the quadratic fit to the peak and to the 3 points on either side of the peak. The definition of λ_T is also shown pictorially. This method of determining the Taylor microscale is applied to experiments at all times available, including those for which the mixing layer is clearly not turbulent, and is referred to as λ_T for all cases.

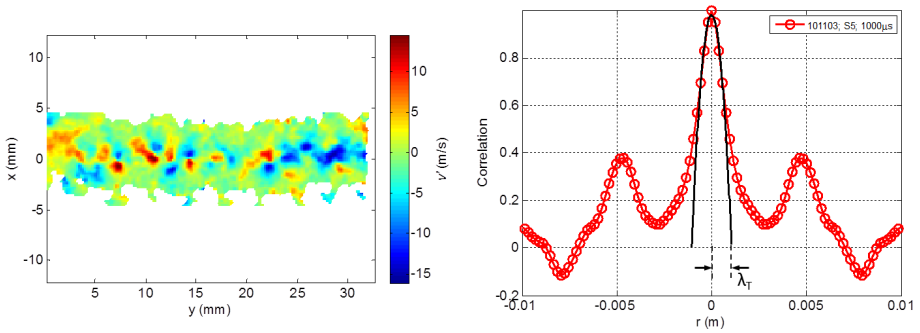

FIG. 10. Example of autocorrelation method for measuring λ_T using v'. Example is for a Mach 1.5 experiment at $t = 1000\mu$s.

Figure 11 compares the autocorrelation of ρ' at the streamwise center of mass between each Mach number at 6 different scaled times. At the earliest time shown, the autocorrelations for each Mach number are very similar, with peaks at every half wavelength $n\frac{\lambda_0}{2}$ (where the primary wavelength $\lambda_0 = 3.6$ mm and $n = 1, 2, 3...$). As seen in the concentration maps of Figure 1, more small scale mixing is observed sooner in Mach 1.50 experiments near the vortex cores. This is also observed quantitatively in the autocorrelations as the peak at $\lambda/2$ shrinks and disappears by the third time while it still remains for Mach 1.21 and 1.36. In general, for each Mach number case the strong spanwise periodicity weakens overtime, but some signatures of the initial conditions persist even at late times.

Figure 12 compares streamwise center autocorrelations for ρ' (color) *vs* v' (black) using simultaneously acquired fields. Columns compare for different Mach number, and rows for different scaled time. At the earliest time shown, peaks at $\lambda_0/2$ are observed for ρ', but a strong negative correlation is observed for v'. At this stage in the growth, with counter-rotating vortices forming for each half wavelength (negative velocity correlations) it is clear from the autocorrelations how the velocity field transports the scalar density field. As time progresses the flow becomes more complex, and molecular mixing through diffusion occurs, so such a direct relationship between the velocity and density correlations is not as clear at intermediate and late times. Mach 1.21 experiments also exhibit less negative correlation in v' at intermediate and late times. This is likely because the vortex cores lag behind the streamwise center of the mixing layer, and therefore the fluctuations are not as strong or as structured as they are at the streamwise center of higher Mach number cases.

Figure 13 shows the evolution of the $\lambda_{T,v}(x)$ with time for each Mach number case.

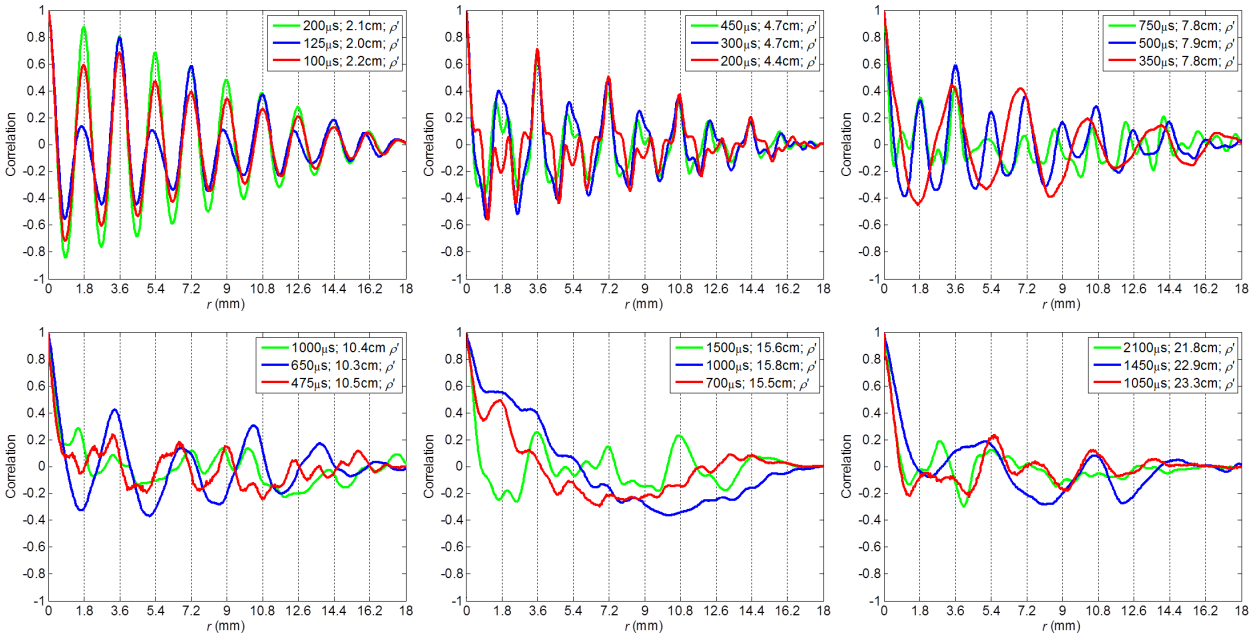

FIG. 11. Mach number comparison of spanwise autocorrelations of ρ' at the center of mass location. Tick marks indicate every half perturbation wavelength.

In general, $\lambda_{T,v}$ tends to increase over time for each Mach number, usually a signature of decreasing Re and possible decaying turbulence. Mach 1.21 experiments develop an asymmetric profile over time with higher $\lambda_{T,v}$ occurring on the downstream side of the structure. Again, this appears to be a result of lagging vortex cores in those experiments, and smaller fluctuations on the downstream side as a result. $\lambda_{T,v}$ for Mach 1.36 and 1.50 experiments are fairly symmetric and develop a peak at the center of the layer at earlier times. But as time progresses, no clear structure emerges, and the symmetry appears to be lost. These features can also be observed in Figure 14, where $\lambda_{T,v}$ is compared between Mach number at 6 different scaled times. Here, it can be seen that low Mach number produces significantly higher values for $\lambda_{T,v}$ in certain regions of the mixing layer than the two higher Mach numbers. Mach 1.21 has the lowest fluctuations in velocity and the weakest vortex structures, and so correlations in the near field in certain regions tend to be higher, leading to a spreading in the local autocorrelation peak. The higher Mach numbers develop an intermediate time peak at the center of the mixing layer where the centers of the vortex cores tend to be. At this location, the spanwise component of velocity is not strongly varying and so the near field correlations are higher. At the latest times, higher Mach numbers show less streamwise asymmetry than the Mach 1.21 case.

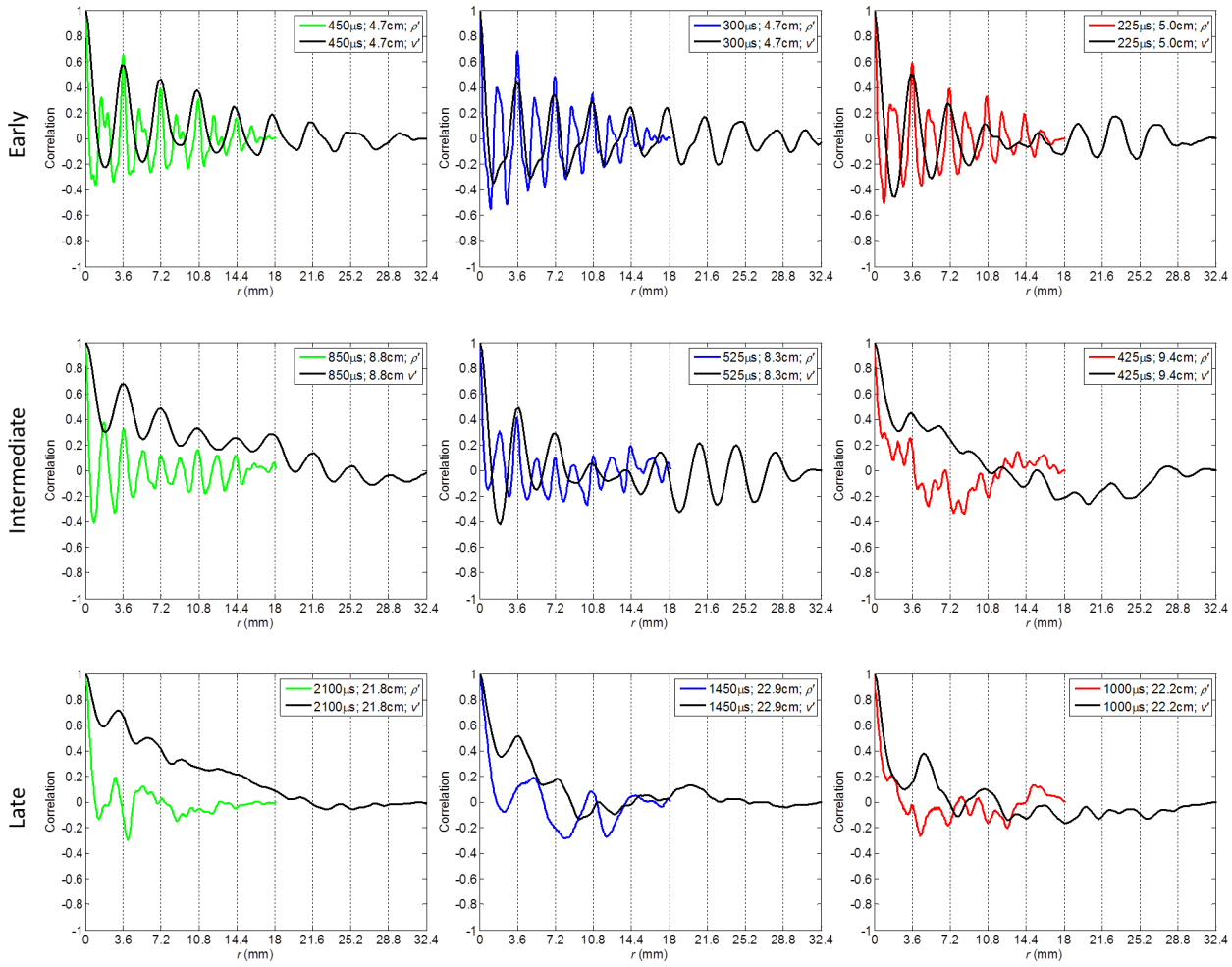

FIG. 12. Comparison of spanwise autocorrelations at the streamwise center for simultaneously acquired v and ρ fields.

In Figure 15, we compare $\lambda_{T,\rho}$ and $\lambda_{T,v}$ using simultaneously acquired ρ and v fields. Columns differentiate Mach number, and rows show for experiments at similar scaled time. For each Mach number, at all times and at all positions throughout the mixing layer, λ_T from velocity is higher than that from density. The streamwise profiles for these two different measurements also do not appear to be very well correlated. This highlights the degree to which different estimates of λ_T can be for experimental data depending on the field (velocity or density) that is used, and the location in the flow that is measured.

Figure 16 shows λ_T for each Mach number using five different methods: 1) $\lambda_{T,v}$ at the streamwise center, 2) $\lambda_{T,u}$ at the streamwise center, 3) $\lambda_{T,\rho}$ at the streamwise center, 4) λ_T using a Reynolds number scaling ($\lambda_T = \sqrt{10}\delta Re^{-1/2}$)[41] based on Re_Γ for $x < 13$ cm, and 5) λ_T using the same Reynolds number scaling but based on Re_K for $x > 13$ cm. Measurements

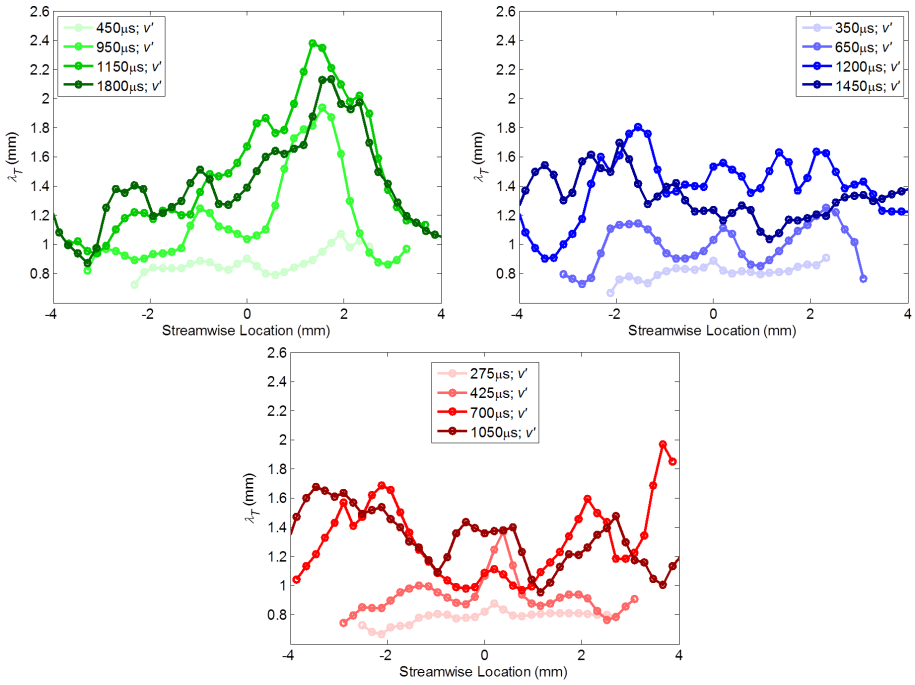

FIG. 13. Time evolution of $\lambda_{T,v}$ as a function of streamwise position across the mixing layer for each Mach number from spanwise autocorrelations.

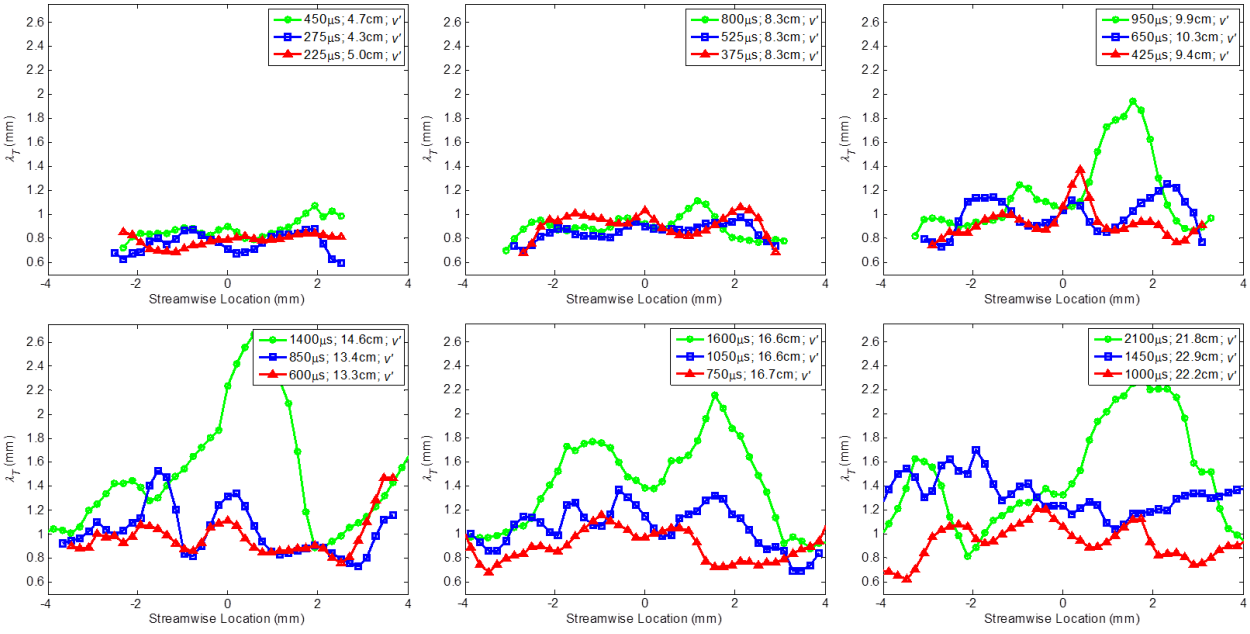

FIG. 14. Mach number comparison of $\lambda_{T,v}$ as a function of streamwise position from spanwise autocorrelations. Each plot compares between Mach numbers at a similar scaled time x.

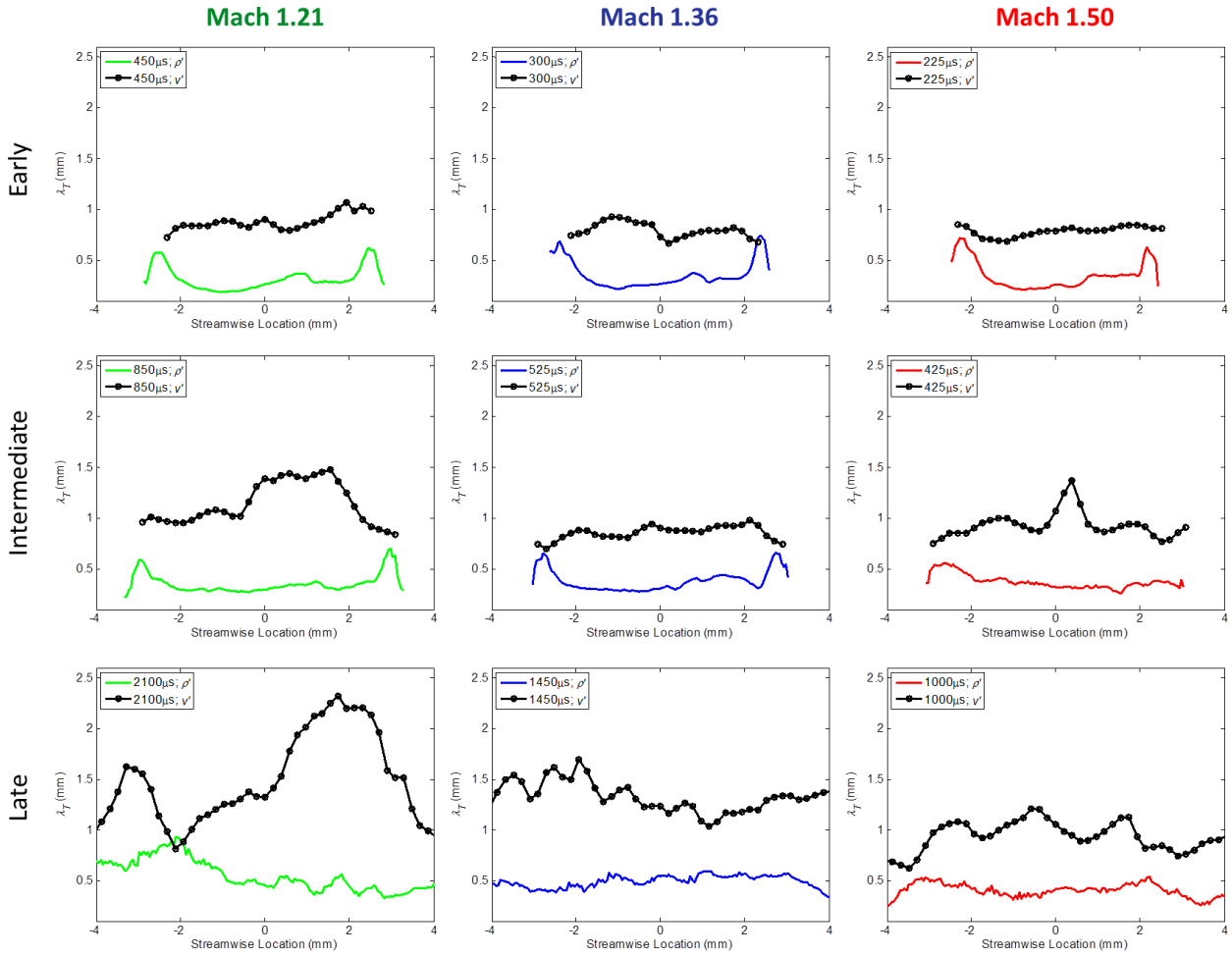

FIG. 15. Comparison of λ_T derived from spanwise autocorrelations as a function of streamwise position from simultaneously acquired v and ρ maps.

of $\lambda_{T,v}$ are a factor of three or more higher than $\lambda_{T,\rho}$. Measurements of λ_T using the Re_Γ scaling tend to be lower than those estimated directly from ρ' over most intermediate times. Measurements of λ_T using the Re_K scaling agree better with those from ρ' throughout the late time regime, but are in the best agreement at the latest times. A new Reynolds number scaling that we find in best agreement with the velocity based Taylor microscale in this particular flow is $\lambda_T = 10\delta Re^{-1/2}$.

An interesting transition is observed in $\lambda_{T,\rho}$ at $x = 6$ cm, just as the flow transitions from early to intermediate times. It is at this time that a dramatic increase in small scale mixing is observed in the vortex cores for all three cases. The sharp upturn of $\lambda_{T,\rho}$ at this time seems to clearly mark this transition. Furthermore, that this occurs at the same downstream location for each Mach number is additional validation that the time scaling of $x = \Delta u\, t$ is

effective in collapsing similar mixing development between Mach numbers.

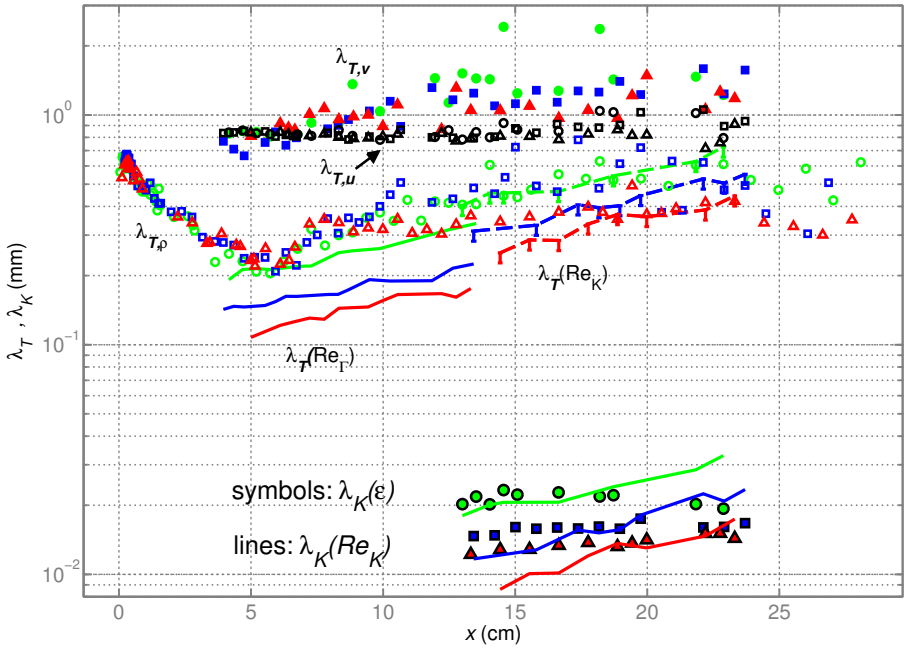

FIG. 16. Estimates of $\lambda_{T,v}$, $\lambda_{T,u}$, and $\lambda_{T,\rho}$ from spanwise autocorrelation at the streamwise center, and inferred from Reynolds number scaling using both Re_Γ and Re_K. Also shown are estimates of $\lambda_K(\epsilon)$ and λ_K inferred from a Reynolds number scaling using $\lambda_K = \delta Re_K^{-3/4}$. (green/circles: M = 1.21; blue/squares: M = 1.36; red/triangles: M = 1.50)

The Taylor microscale ratios $\lambda_{T,v}/\lambda_{T,u}$ and $\lambda_{T,v}/\lambda_{T,\rho}$ are shown in Figure 17. The ratio of longitudinal to transverse Taylor microscales ($\lambda_{T,v}/\lambda_{T,u}$) is $\sqrt{2}$ in isotropic turbulence[41]. We find this ratio to increase throughout early and intermediate times until reaching a plateau of around $\sqrt{2}$ at late times, providing further evidence of a transition in the flow towards turbulence. The ratio of velocity to density Taylor microscales is useful in quantifying the time scales over which turbulent energy is dissipated compared to scalar dissipation through molecular diffusion[42,43]. We find $\lambda_{T,v}/\lambda_{T,\rho} = 3$ on average, with linear fits to the data showing a slight negative trend in time for each Mach number.

In homogeneous, isotropic turbulence, the longitudinal and transverse velocity Taylor microscales can also be defined, respectively, as

$$\lambda_{T,u_i}^2 = 2\,\overline{u_i'^2}/\,\overline{(\partial u_i/\partial x_i)^2} \quad , \quad \lambda_{T,u_i}^2 = \overline{u_i'^2}/\,\overline{(\partial u_i/\partial x_j)^2} \qquad (i \neq j), \tag{7}$$

and the density Taylor microscale can be defined as

$$\lambda_{T,\rho}^2 = \overline{\rho'^2}/\,\overline{(\partial \rho/\partial x_i)^2}. \tag{8}$$

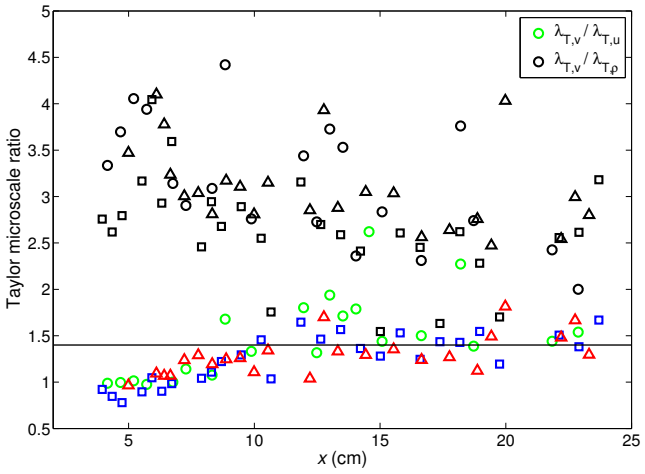

FIG. 17. The ratios $\lambda_{T,v}/\lambda_{T,u}$ (color symbols) and $\lambda_{T,v}/\lambda_{T,\rho}$ (black symbols). The horizontal line marks $\sqrt{2}$.

In Figure 18 the Taylor microscale computed from the curvature of autocorrelations at $R(0)$, as in Eq. 6, is compared to results from Eqs. 7 and 8 for late times when there is more support for isotropy assumptions. The estimations from Eqs. 7 and 8 provide an independent check of the Taylor microscale determined from the autocorrelations. For $\lambda_{T,u}$ and $\lambda_{T,v}$ the two methods agree very well on average. For $\lambda_{T,\rho}$ the estimates from Eq. 8 are 50% lower on average. These results give us confidence in our estimates of the Taylor microscale within the precision required for our conclusions.

A Taylor Reynolds number, Re_T can be defined using λ_T, and the velocity fluctuation level, u'_{rms} as,

$$\mathrm{Re}_T = \frac{u'_{rms}\lambda_T}{\nu}. \tag{9}$$

Here $u'_{rms} = \sqrt{(\langle u'^2\rangle + \langle v'^2\rangle)/2}$ is the RMS of all velocity fluctuations in both streamwise and spanwise directions as computed from ensemble averaging, and $\lambda_T = \lambda_{T,v}$. Figure 19 shows Re_T for each time that ensemble averages were available. Using instantaneous spatial averages for u'_{rms} agree with these results to within 15%. For comparisons available at similar downstream locations, Re_T is higher with increasing Mach number. Dimotakis[9] suggests that fully developed turbulent flow requires $\mathrm{Re}_T > 100$ to be sustained. This requirement is met by each Mach number for all times measured using $\lambda_{T,v}$. Note that if we use $\lambda_{T,\rho}$, Re_T values would be approximately divided by three.

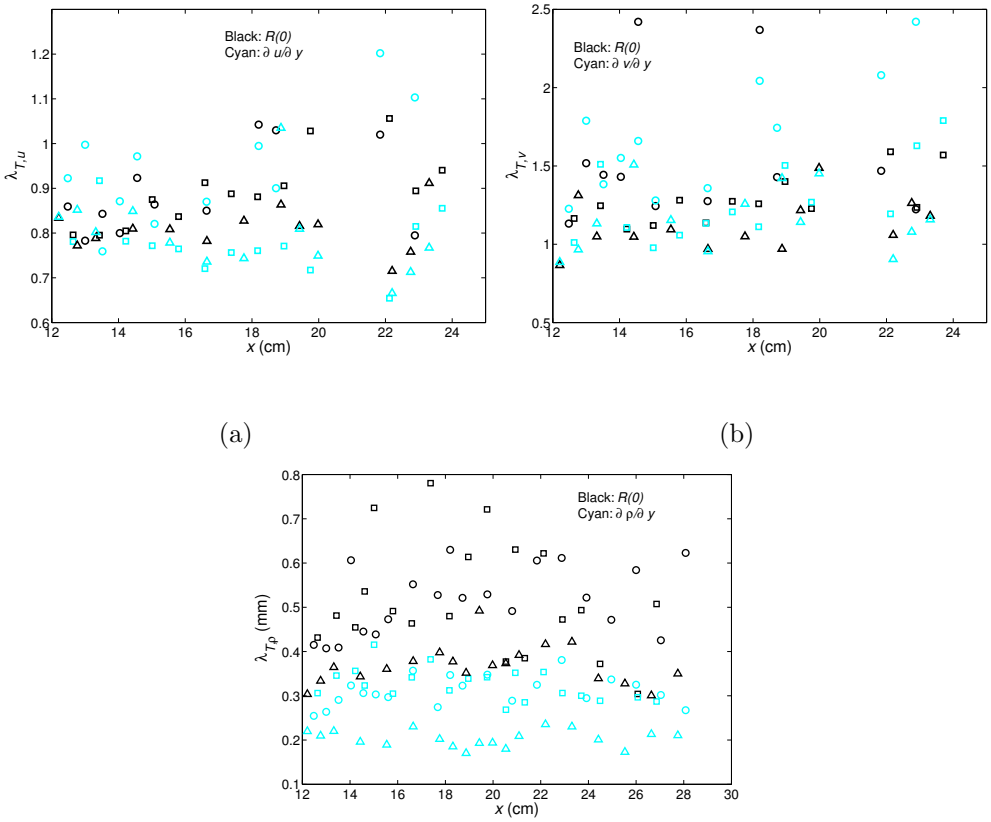

FIG. 18. Comparison of methods for estimating (a) $\lambda_{T,u}$, (b) $\lambda_{T,v}$ and (c) $\lambda_{T,\rho}$ using autocorrelations (black), and spatial gradients (cyan).

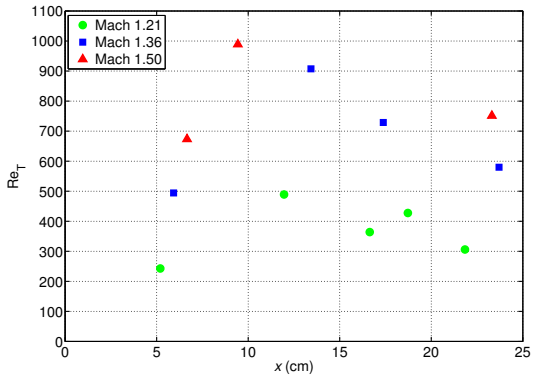

FIG. 19. Re_T computed from $\lambda_T(v')$ as a function of streamwise position for each Mach number for times at which ensemble averages were available.

2. *Dissipation and Kolmogorov scale*

Following a similar procedure to that used in Tomkins *et al.*[16], we obtain initial estimates for dissipation,

$$\epsilon = \nu \overline{\frac{\partial u_j}{\partial x_i}\left(\frac{\partial u_i}{\partial x_j} + \frac{\partial u_j}{\partial x_i}\right)}, \tag{10}$$

from the two available velocity components as a function of time and Mach number. Local isotropy is assumed where necessary for the out of plane component, therefore we limit discussion of these measurements to late times where this assumption is supported by the similarity of fluctuations between the two measured velocity components (as shown in Figures 3, 4, and 5). Furthermore, out of plane isotropy was observed in the large-eddy simulations reported by Gowardhan and Grinstein[24] using similar initial conditions and a Mach 1.2 shock wave. For isotropic turbulence, dissipation can also be defined as $\epsilon = \frac{15\nu u'^2}{\lambda_T^2}$, where λ_T is the transverse Taylor microscale ($\lambda_{T,u}$ for our case). This alternate definition of ϵ provides a check of our estimates using Eq. 10, and we find agreement between the two measures to within 50%. From the dissipation, the Kolmogorov scale, λ_K can then be estimated as,

$$\lambda_K = \left(\frac{\nu^3}{\epsilon}\right)^{1/4}. \tag{11}$$

The initial estimates of ϵ and λ_K can then be corrected for under-resolved PIV data following Antonia *et al.*[44]. The average initial estimate for the Kolmogorov scale over all Mach numbers at late times is $\overline{\lambda_{K,0}} = 21$ μm. With a vector spacing of 193 μm, we find a dimensionless resolution of $\Delta x^* = \Delta x/\overline{\lambda_{K,0}} \approx 9$. Due to this resolution limit, initial estimates of dissipation are $\sim$60% that of their true value according to Antonia *et al.*[44]. Corrected values of dissipation for the latest times for each M are $\epsilon \approx \mathcal{O}(10^4)$ m^2/s^3. Corrected λ_K values using the corrected dissipation are shown in Figure 16, along with the various estimates of λ_T. Compared at the same streamwise location, λ_K is smaller with increasing Mach number. The average estimate for the corrected Kolmogorov scale over all late times and Mach numbers is $\overline{\lambda_K} = 17$ μm, so correcting the dissipation only has a 2% effect on the final values. Values for λ_K (shown in Figure 16) are about 2 orders of magnitude lower than $\lambda_{T,v}$. A Reynolds number scaling[9] $\lambda_K = \delta Re_K^{-3/4}$ is also shown, and agrees remarkably well with the λ_K estimates.

3. Inner viscous and Liepmann-Taylor scales

Another criterion proposed for turbulent mixing is that the Liepmann-Taylor scale be greater than the inner viscous scale ($\lambda_L/\lambda_\nu > 1$) for an inertial range to be possible[9]. Both length scales can be estimated using Re such that[9],

$$\lambda_\nu = 50\delta \mathrm{Re}^{-3/4} \quad , \quad \lambda_L = 5\delta \mathrm{Re}^{-1/2}. \tag{12}$$

When defined this way, $\lambda_L/\lambda_\nu = 1$ is equivalent to $\mathrm{Re} = 10^4$. These scales can also be estimated through their relationship to the Kolmogorov scale and Taylor microscale as,

$$\lambda_\nu = 50\lambda_K \quad , \quad \lambda_L = \begin{cases} 5\lambda_T \\ 2.2\lambda_T \\ 1.6\lambda_T \end{cases} \tag{13}$$

where the relationship for λ_ν has been found for a variety of flows[45], and the various relationships for λ_L are found in or inferred from other sources[9,11,41]. The evolution of λ_L/λ_ν calculated several different ways is shown in Figure 20. Values for $\lambda_L/\lambda_\nu \approx 1$ are obtained using the Reynolds number scaling based on both Γ and K (from Eq. 12), but $\lambda_L/\lambda_\nu \approx 8$, 3.5, or 2.3 based on the measured values of $\lambda_{T,v}$ and λ_K depending on the relationship used for λ_L in Eq. 13. This discrepancy of nearly an order of magnitude in λ_L/λ_ν is quite large as from Eq. 12 it implies a Reynolds number, $\mathrm{Re} = (10\lambda_L/\lambda_\nu)^4$, discrepancy of three orders of magnitude between the different methods. No matter which definition of λ_L is used, the lack of consistency calls into question the Reynolds number scaling in Eq. 12, and suggests that it may not be appropriately applied to R-M flows. Lombardini *et al.*[12] suggest that sufficient inertial range for full scale turbulence requires a decade of scales ($\lambda_L/\lambda_\nu \geq 10$), and that only occurs for $M \geq 3$ in their single interface large-eddy simulations. Depending on how λ_L/λ_ν is estimated in the current experiment, we could conclude that the flow is either undergoing a mixing transition but not turbulent, or that it has sufficient scale separation for fully developed turbulence. Clearly, more experimental data in which both velocity and density are measured would greatly advance our understanding and help resolve the best ways to quantify the mixing behavior and determine possible scaling laws for RMI flows.

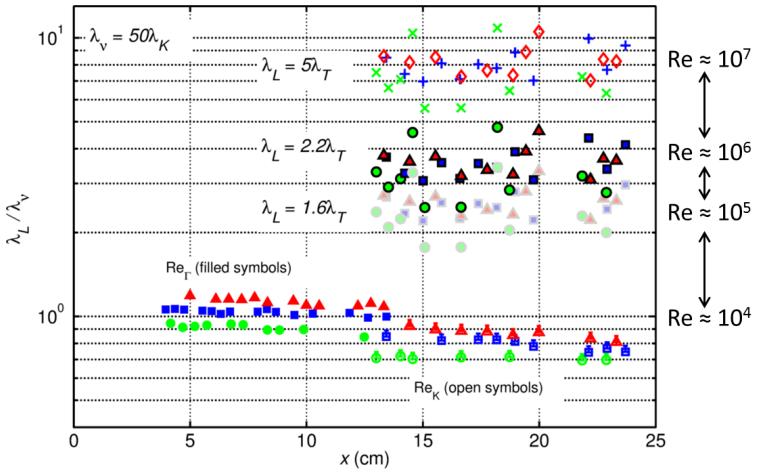

FIG. 20. λ_L/λ_ν as a function of downstream position based on Re_Γ, Re_K, and measured values of λ_K and λ_T.

E. Density-specific-volume correlation

The density-specific-volume correlation, b, appears as an unclosed multiplier in the production term of the mass flux equation for variable density flows and can be defined using fluctuating or mean density fields as[46]

$$b = \overline{-\rho' \left(\frac{1}{\rho}\right)'} = \bar{\rho}\,\overline{\left(\frac{1}{\rho}\right)} - 1. \tag{14}$$

b is one of the evolved quantities in the Reynolds-averaged Navier-Stokes (RANS) turbulence model used at Los Alamos National Laboratory (named 'BHR' for Besnard-Harlow-Rauenzahn)[46,47] but because it is unclosed, experimental validation data is required to know when and how to initialize the turbulence model. With high resolution quantitative PLIF imaging, our experiments are able to bound the initial value of b. The average value, $\langle b \rangle$, amongst all available density maps at a given time is presented in Figure 21a. The calculation of $\langle b \rangle$ and its use for quantifying the uniformity of mixing are discussed in detail in Orlicz *et al.*[19]. Here, we reiterate the plateau feature seen at the $4.5 \leq x \leq 6.5$ cm for each Mach number near the transition from early to intermediate times. This feature appears to be a result of small-scale mixing in the vortex cores and occurs at the same time as the minimum observed for $\lambda_{T,\rho}$ measurements in Figure 16, providing further indication that the flow is undergoing a real transition in mixing at this scaled time. Just after the plateau, in the range of $7 \leq x \leq 13$ cm, the average value of $\langle b \rangle$ is $18{\times}10^{-3}$, $15{\times}10^{-3}$ and $5{\times}10^{-3}$

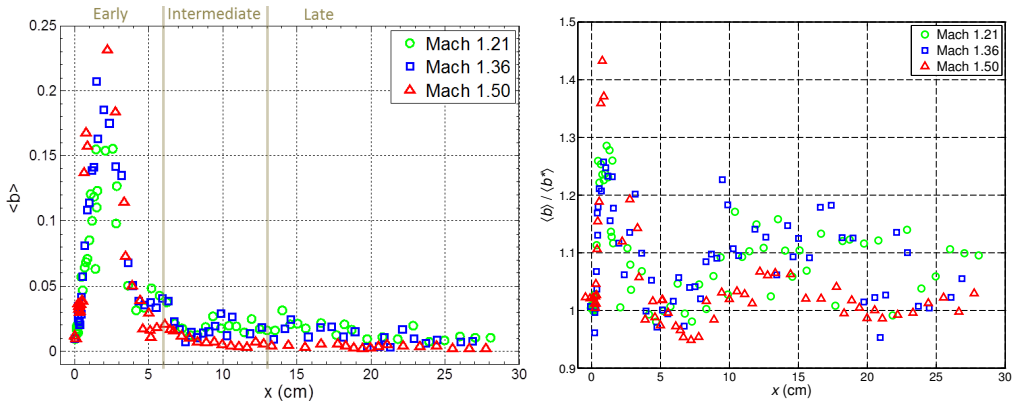

(a) (b)

FIG. 21. (a) $\langle b \rangle$ as a function of position, and (b) the ratio $\langle b \rangle / \langle b^* \rangle$ showing the applicability of the Boussinesq approximation as time progresses.

for $M = 1.21$, 1.36, and 1.50, respectively.

The Boussinesq approximation is often made to simplify the governing equations for variable density flows. In the limit of small density fluctuations the Boussinesq approximation is valid and the density-specific-volume correlation can be expressed as[48],

$$b^* = \frac{\overline{(\rho')^2}}{\overline{\rho}^2}. \tag{15}$$

To assess the validity of the Boussinesq approximation, we plot $\langle b \rangle / \langle b^* \rangle$ in Figure 21b. Over most times this approximation leads to a slight under-estimation of the density-specific-volume correlation, with the highest discrepancy occurring at early times when the density fluctuations are the highest before much molecular mixing has taken place. There are also a few times for which $\langle b \rangle / \langle b^* \rangle < 1$. Both b and b^* were calculated only for the middle 20% region of the mixing layer as discussed in Orlicz[19]. The density fluctuations at the edges of the mixing layer tend to be higher and therefore sometimes produce higher values of b if included (as seen in previous experimental work[1613]). In the current experiments, the edges only produce a higher $\langle b \rangle / \langle b^* \rangle$ at early times, but for the majority of times the Boussinesq approximation produces a 20% or less error, independent of the location within the mixing layer.

F. Power spectral density

We further characterize the ranges of length scales present in the flow by investigating the power spectral density (PSD) of the density field. Figure 22 shows the PSD of the initial conditions and three different scaled post-shock times for each Mach number. The energy content for the initial conditions has a steep drop off below the primary wavelength ($\lambda_0 = 3.6$ mm). Shortly after shock passage, the power spectra dramatically change. As the perturbations start to grow, a strong peak develops at $\lambda_0/2$ for each Mach number, as shown in the early time PSD. The $\lambda_0/2$ peak is maintained during intermediate times when the mixing layer is still dominated by the counter-rotating vortex pairs. As mixing continues and the flow breaks down to smaller scales, the spectra smooth out for all wavenumbers and no strong peak for λ_0 or $\lambda_0/2$ is observed at late times. The slope of the late time spectra approaches $k^{-5/3}$ over approximately one decade of scales.

The PSD plots consistently show more activity at high wavenumbers than the power-law scaling would predict. This feature is especially prominent at early times. While a follow-up study focused on small scales will be required to provide a better understanding of the physics involved, this behavior may be suggestive of extra activity on the small scales due to the presence of the particle tracer. It has been suggested[49] that the latter may affect the development of small-scale instabilities in transition to turbulence and, depending on the conditions, either advance or suppress their growth. However, this subject is beyond the scope of the current study.

The approximate wavenumber of each of the turbulent length scales is also shown for reference for late times to give a sense of the scale separation. Here, λ_K is estimated using dissipation, with $\lambda_\nu = 50\lambda_K$, and the spanwise velocity is used for the Taylor microscale $\lambda_T = \lambda_{T,v}$, with $\lambda_L = 2.2\lambda_T$.

IV. CONCLUSIONS

In our shock-driven variable-density mixing experiments, we have shown evidence of mixing transition for multiple Mach numbers using the velocity fluctuation PDFs, the similarity of $\overline{K}$ estimates using ensemble and spatial averages, the ratio of longitudinal to transverse Taylor microscales $\lambda_{T,v}/\lambda_{T,u} = \sqrt{2}$, a Taylor Reynolds number exceeding 100, a power spec-

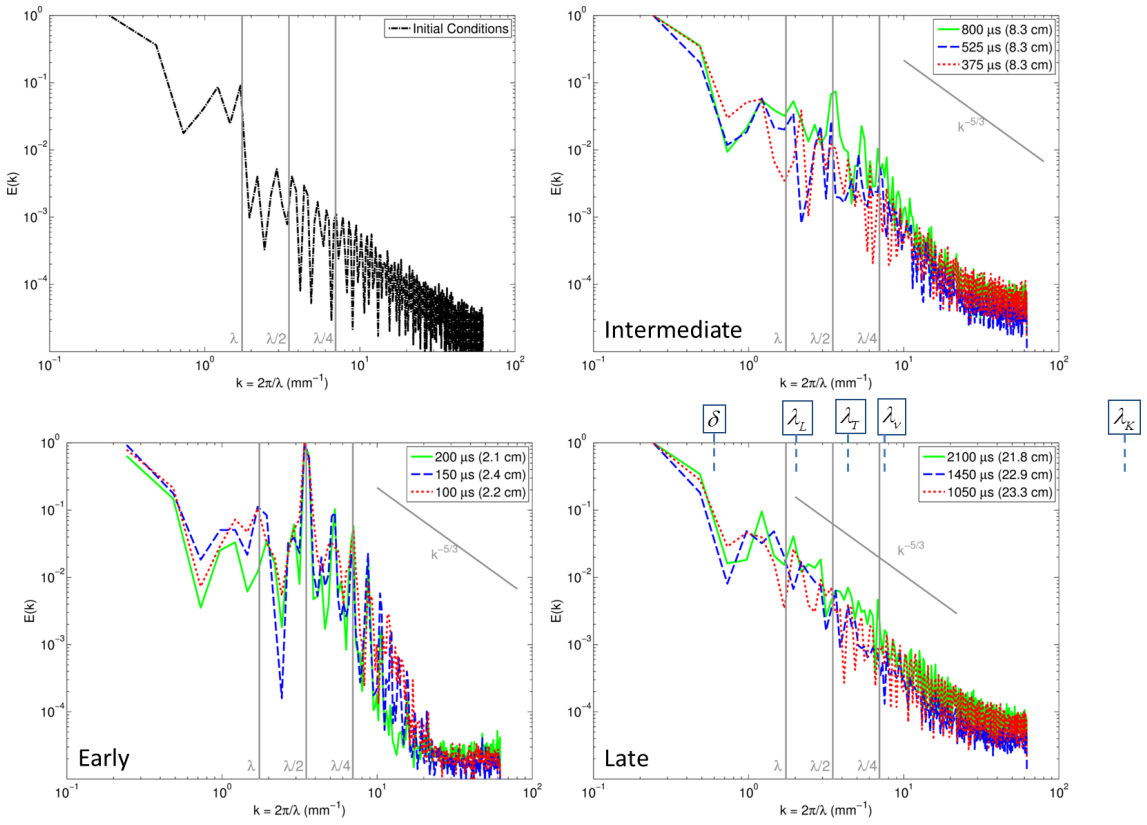

FIG. 22. PSD of density fields for the initial conditions, and 3 scaled times for each Mach number: early, intermediate, and late. Vertical lines indicate the primary wavelength, λ_0, $\lambda_0/2$, and $\lambda_0/4$ for orientation. A $k^{-5/3}$ slope is also shown on each post-shock plot for reference.

tra approaching a $k^{-5/3}$ slope, and a visual inspection of the PLIF images. Yet, only Mach 1.36 and Mach 1.50 experiments meet the criterion of $\mathrm{Re}_\Gamma > 10^4$.

Scaling time using $x = \Delta u\, t$ is a very good way of comparing physical mixing quantities among different Mach numbers. This was previously observed in Orlicz *et al.*[19] for density related quantities and also works for the velocity related quantities as well.

Indications of two mixing transitions were found for each Mach number. The first occurs at a scaled time of x=6 cm when small scale mixing begins to occur in the vortex cores where the velocity field has stretched and folded the scalar density field the most. Heightened mixing through molecular diffusion along the density gradients in these regions is observed at this time. This transition is seen quantitatively in the dramatic upturn in the density Taylor microscale ($\lambda_{T,\rho}$), and in the plateau feature seen in the density-specific-volume correlation ($\langle b \rangle$). This transition is not obvious from the velocity field, but the first available data

points for velocity only occur at 5 cm, making it difficult to identify a trend. The second transition occurs at 13 cm and marks the point at which the flow begins exhibiting isotropy and some of the signatures of turbulence listed above. Memory of the initial conditions is still retained at late times at the wavelength of the initial perturbations as evidenced qualitatively by the persistence of features at the primary wavelength in the concentration maps and quantitatively by peaks in the autocorrelations, but several of the quantities measured show a trend toward local homogeneous, isotropic turbulence for each Mach number.

The Taylor microscale for density, and the two measured components of velocity are estimated in two ways: from the curvature of autocorrelations and from spatial gradients. The agreement between the two methods gives confidence in those values, and the ones obtained for the Taylor Reynolds number, Re_T = 300, 600, and 800 for the latest times for M = 1.21, 1.36, and 1.50 respectively. While the Reynolds number scaling $\lambda_{T,\rho} = \sqrt{10}\delta \mathrm{Re}_K^{-1/2}$ agrees well with our measurements for the density Taylor microscale, a new scaling of $\lambda_{T,u} = 10\delta \mathrm{Re}_K^{-1/2}$ is in better agreement with those measured from the velocity field.

From estimates of the Taylor microscale and the Kolmogorov scale, we obtain the ratio of Liepmann-Taylor and inner viscous scales, and find significant differences between those values and ones given by Reynolds number scaling[9] suggesting that this scaling may not be appropriate for this flow. Open questions that remain include how Reynolds number should be measured at each stage of these unsteady, transitional flows, whether there is a universal Reynolds number that is a reliable indication of turbulence for flows of this nature, and whether there exist universal Reynolds number scaling laws for various turbulent length scales.

ACKNOWLEDGMENTS

The authors would like to acknowledge the contribution of Dr. Ricardo Mejia-Alvarez in offering his expertise in data analysis and turbulence, and for valuable discussions regarding the results presented here. We would also like to thank Dr. Raymond Ristorcelli for many useful discussions and suggestions that helped to strengthen this work.

REFERENCES

[1]R. D. Richtmyer. Taylor instability in shock acceleration of compressible fluids. *Communications on Pure and Applied Mathematics*, 13:297–319, 1960.

[2]Ye. Ye. Meshkov. Instability of a shock wave accelerated interface between two gases. Technical Report NASA TT F-13074, NASA Technical Translation, 1970.

[3]W. D. Arnett, J. N. Bahcall, R. P. Kirshner, and S. E. Woosley. Supernova 1987a. *Annual Review of Astronomy and Astrophysics*, 27:629–700, 1987.

[4]C. C. Wu and P. H. Roberts. Richtmyer-Meshkov instability and the dynamics of the magnetosphere. *Geophysical Research Letters*, 26(6):665–658, 1999.

[5]W.J. Hogan, R. Bangerter, and G.L. Kulcinski. Energy from inertial fusion. *Physics Today*, 45:42–50, 1992.

[6]J. Lindl. Development of the indirect-drive approach to inertial confinement fusion and the target physics basis for ignition and gain. *Physics of Plasmas*, 2(11):3933–4024, 1995.

[7]J. Yang, T. Kubota, and E. E. Zukoski. Applications of shock-induced mixing to supersonic combustion. *AIAA Journal*, 31(5):854–862, 1993.

[8]P. E. Dimotakis. Turbulent mixing. *Annual Review of Fluid Mechanics*, 37:329–356, 2005.

[9]P. Dimotakis. The mixing transition in turbulent flows. *Journal of Fluid Mechanics*, 409:69–98, 2000.

[10]H. F. Robey, Y. Zhou, A. C. Buckingham, P. Keiter, B. A. Remington, and R. P. Drake. The time scale for the transition to turbulence in a high Reynolds number, accelerated flow. *Physics of Plasmas*, 10(3):614 – 22, MAR 2003.

[11]Y. Zhou, B. A. Remington, H. F. Robey, A. W. Cook, S. G. Glendinning, A. Dimits, A. C. Buckingham, G. B. Zimmerman, E. W. Burke, T. A. Peyser, W. Cabot, and D. Eliason. Progress in understanding turbulent mixing induced by Rayleigh-Taylor and Richtmyer-Meshkov instabilities. *Physics of Plasmas*, 10:1883–1896, 2003.

[12]M. Lombardini, D. Pullin, and D. Meiron. Transition to turbulence in shock-driven mixing: a Mach number study. *Journal of Fluid Mechanics*, 690:203–226, 2012.

[13]B. Balakumar, G. Orlicz, J. Ristorcelli, S. Balasubramanian, K. Prestridge, and C. Tomkins. Turbulent mixing in a Richtmyer-Meshkov fluid layer after reshock: velocity and density statistics. *Journal of Fluid Mechanics*, 696:67–93, 2012.

[14]C. Weber, N. Haehn, J. Oakley, D. Rothamer, and R. Bonazza. Turbulent mixing measurements in the Richtmyer-Meshkov instability. *Physics of Fluids*, 24:074105, 2012.

[15]S. Balasubramanian, G. Orlicz, and K. Prestridge. Experimental study of initial condition dependence on turbulent mixing in shock-accelerated Richtmyer-Meshkov fluid layers. *Journal of Turbulence*, 14(3):170–196, 2013.

[16]C. Tomkins, B. Balakumar, G. Orlicz, and K. Prestridge. Evolution of the density self-correlation in developing Richtmyer-Meshkov turbulence. *Journal of Fluid Mechanics*, 735:288–306, 2013.

[17]C. Weber, N. Haehn, J. Oakley, D. Rothamer, and R. Bonazza. An experimental investigation of the turbulent mixing transition in the Richtmyer-Meshkov instability. *Journal of Fluid Mechanics*, 748:457–487, 2014.

[18]D. Reilly, J. McFarland, M. Mohaghar, and D. Ranjan. The effects of initial conditions and circulation deposition on the inclined-interface reshocked Richtmyer-Meshkov instability. *Experiments In Fluids*, 56:168, 2015.

[19]G. Orlicz, S. Balasubramanian, and K. Prestridge. Incident shock Mach number effects on Richtmyer-Meshkov mixing in a heavy gas. *Physics of Fluids*, 25:114101, 2013.

[20]S. Balasubramanian, G. Orlicz, K. Prestridge, and B. Balakumar. Experimental study of initial condition dependence on Richtmyer-Meshkov instability in the presence of reshock. *Physics of Fluids*, 24:034103, 2012.

[21]D. J. Hill, C. Pantano, and D. I. Pullin. Large-eddy simulation and multiscale modelling of a Richtmyer-Meshkov instability with reshock. *Journal of Fluid Mechanics*, 557:29–61, 2006.

[22]M. Hahn, D. Drikakis, D. L. Youngs, and R. J. R. Williams. Richtmyer-Meshkov turbulent mixing arising from an inclined material interface with realistic surface perturbations and reshocked flow. *Physics of Fluids*, 23:046101, 2011.

[23]M. Lombardini, D. J. Hill, D. I. Pullin, and D. I. Meiron. Atwood ratio dependence of Richtmyer-Meshkov flows under reshock conditions using large-eddy simulations. *Journal of Fluid Mechanics*, 670:439–480, 2011.

[24]A. A. Gowardhan and F. F. Grinstein. Numerical simulation of Richtmyer-Meshkov instabilities in shocked gas curtains. *Journal of Turbulence*, 12(23):1–24, 2011.

[25]B. Thornber, D. Drikakis, D. L. Youngs, and R. J. R. Williams. The influence of initial conditions on turubulent mixing due to Richtmyer-Meshkov instability. *Journal of Fluid Mechanics*, 654:99–139, 2010.

[26]J. A. McFarland, D. Reilly, W. Black, J. Greenough, and D. Ranjan. Modal interactions between a large-wavelength inclined interface and small-wavelength multimode perturbations in a Richtmyer-Meshkov instability. *Physical Review E*, 92:013023, 2015.

[27]O. Schilling and M. Latini. High order weno simulations of three-dimensional reshocked Richtmyer-Meshkov instability to late times: dynamics, dependence on initial conditions, and comparisons to experimental data. *Acta Mathematica Scientia*, 30:595–620, 2010.

[28]D. Livescu and R. Ristorcelli. Variable-density mixing in buoyancy-driven turbulence. *Journal of Fluid Mechanics*, 605:145–180, 2008.

[29]B. J. Balakumar, G. C. Orlicz, C. D. Tomkins, and K. P. Prestridge. Simultaneous particle-image velocimetry-planar laser-induced fluorescence measurements of Richtmyer-Meshkov instability growth in a gas curtain with and without reshock. *Physics of Fluids*, 20:124103, 2008.

[30]R. Adrian. Particle-imaging techniques for experimental fluid mechanics. *Annual Review of Fluid Mechanics*, 23:261–304, 1991.

[31]A. K. Prasad, R. J. Adrian, C. C. Landreth, and P. W. Offutt. Effect of resolution on the speed and accuracy of particle velocimetry interrogation. *Experiments in Fluids*, 13:105–116, 1992.

[32]S. Elghobashi. On predicting particle-laden turbulent flows. *Applied Scientific Research*, 52:309–329, 1994.

[33]P. M. Rightley, P. Vorobieff, and R. F. Benjamin. Evolution of a shock-accelerated thin fluid layer. *Physics of Fluids*, 9(6):1770–1782, 1997.

[34]R. Clift and W. H. Gauvin. The motion of particles in turbulent gas streams. *Pro. Chemeca*, 1:14–28, 1970.

[35]M. Parmar, A. Haselbacher, and S. Balachandar. Improved drag correlation for spheres and application to shock-tube experiments. *AIAA*, 48:1273–1276, 2010.

[36]R. Adrian. Dynamic ranges of velocity and spatial resolution of particle image velocimetry. *Measurement Science and Technology*, 8:1393–1398, 1997.

[37]E. Lazar, B. DeBlauw, N. Glumac, C. Dutton, and G. Elliot. A practical approach to PIV uncertainty analysis. In *27th AIAA Aerodynamic Measurement Technology and Ground Testing Conference; 28 June - 1 July, 2010, Chicago, IL*, volume AIAA 2010-4355. AIAA, 2010.

[38]J. J. Charonko and P. P. Vlachos. Estimation of uncertainty bounds for individual particle image velocimetry measurements from cross-correlation peak ratio. *Measurement Science and Technology*, 24:065301, 2013.

[39]J. Jimenez. Intermittency and cascades. *Journal of Fluid Mechanics*, 409:99–120, 2000.

[40]R. Reid, J. Prausnitz, and T. Sherwood. *The properties of gases and liquids.* McGraw-Hill Book Company, New York, 1977.

[41]S. B. Pope. *Turbulent Flows.* Cambridge University Press, Cambridge, United Kingdom, 2000.

[42]J. R. Ristorcelli. Passive scalar mixing: Analytic study of time scale ratio, variance, and mix rate. *Physics of Fluids*, 18:075101, 2006.

[43]A. J. Wachtor, F. F. Grinstein, C. R. DeVore, J. R. Ristorcelli, and L. G. Margolin. Implicit large-eddy simulation of passive scalar mixing in statistically stationary isotropic turbulence. *Physics of Fluids*, 25:025101, 2013.

[44]R. A. Antonia, Y. Zhu, and J. Kim. On the measurement of lateral velocity derivatives in turbulent flows. *Experiments in Fluids*, 15:65–95, 1993.

[45]S. G. Saddoughi and S. V. Veeravalli. Local isotropy in turbulent boundary layers at high Reynolds number. *Journal of Fluid Mechanics*, 268:333–372, 1994.

[46]D. Besnard, F. H. Harlow, R. M. Rauenzahn, and C. Zemach. Turbulence transport equations for variable-density turbulence and their relationship to two-field models. Technical Report LA-12303-MS, Los Alamos National Laboratory, 1992.

[47]J. D. Schwarzkopf, D. Livescu, R. A. Gore, R. M. Rauenzahn, and R. Ristorcelli. Application of second-moment closure model to mixing processes involving multicomponent miscible fluids. *Journal of Tubulence*, 12(49):1–35, 2011.

[48]P. Chassaing, R. A. Antonia, F. Anselmet, L. Joly, and S. Sarkar. *Variable Density Fluid Turbulence.* Kluwer Academic Publishers, Dordrecht, Netherlands, 2002.

[49]C. Poelma, J. Westerweel, and G. Ooms. Particle-fluid interactions in grid-generated turbulence. *Journal of Fluid Mechanics*, 589:315–351, 2007.

View publication stats